Modeling Co-Channel Interference in the THz Band

Jia Ye, *Student Member, IEEE*, Shuping Dang, *Member, IEEE*, Basem Shihada, *Senior Member, IEEE*, and Mohamed-Slim Alouini, *Fellow, IEEE*

***Abstract*—Terahertz (THz) wireless technology is envisioned to enable terabit-per-second (Tbps) and secure transmissions in sixth-generation (6G) communication networks and has attracted attention from academia and industry in recent years. Because the transmission range of THz radios is restricted compared to that of microwave radios, frequency reuses in the THz band become much more flexible and even possible among transceiver pairs in close proximity. However, without appropriate spatial arrangement and coordination, the frequency reuse in the THz band can also lead to severe co-channel interference and result in a low signal-to-interference-plus-noise ratio (SINR) or a signal-to-interference ratio (SIR), which finally degrades signal detection and network reliability. To thoroughly study the co-channel interference in the THz band, we model the co-channel interference by the compound channel model and analyze it in detail. The adopted channel model captures the key features of THz communication, such as, spreading loss, molecular absorption loss, and dynamic shadowing, which is much different and complicated than those used in the low-frequency band. The resulted SINR and SIR are investigated by approximating the sum of co-channel interference as a gamma distribution. The generalized analytical results are also reduced to specialized forms for two special cases, i.e., the single-interferer case and the case of multiple independent and identically distributed (i.i.d.) interferers. Due to the generalized nature of the THz interference model constructed in this paper, the results play a meaningful role in practical implementation and can be easily extended to advanced performance analyses for THz communication systems.**

***Index Terms*—Interference modeling, co-channel interference, signal-to-interference-plus-noise ratio (SINR), signal-to-interference ratio (SIR), terahertz (THz) communications, compound channel model.**

I. Introduction

RECENTLY, the wireless communication community has gradually turned the attention to the beyond fifth-generation (beyond-5G) and sixth-generation (6G) communications, which aim to accommodate terabit-per-second (Tbps) and secure transmission requirements [1]. The utilize of advanced technologies, such as non-orthogonal multiple access (NOMA), index modulation (IM), and smart radios [2]–[4] has greatly improved the spectral efficiency. However, the data transmission volume in the realm of electromagnetic communications is expected to be further boosted in the future networks. One of the favorable approaches is to employ a higher spectrum with more dense network deployment with a shorter coverage [5]. Following the gist of this approach, terahertz (THz) wireless technology and THz communications are being frequently discussed and investigated in both academia and industry [6]–[13].

The latest studies have demonstrated that wireless communications over the THz band can provide unprecedentedly high-speed and physically secure data transmissions at the cost of a much-reduced transmission range. Compared to microwave communications widely utilized in 5G networks, the transmission distance of THz radios is jointly rendered by a higher spreading loss for a higher frequency spectrum by the Friis transmission equation and, more importantly, the molecular absorption loss when propagating through oxygen and water vapor in the atmosphere [10]. Moreover, since the wavelength of THz radio is less than the millimeter level, the THz radio is highly sensitive to human movement between the transmitter and the receiver. This feature leads to dynamic shadowing and further decreases the transmission range of THz communications [14]. Various ray-tracing experimental and simulation platforms have been constructed to understand the exact propagation behaviors of THz radios [15]–[19], These valuable works lay a solid foundation for the combination of THz communications and other advanced wireless technologies, such as, aerial platforms, and reconfigurable reflecting surfaces (RISs) to compose highly efficient communication networks [20]–[22].

From an engineering perspective, any technological feature can become a double-edged sword, and the highly restricted transmission range of THz communications is not an exception. Although the use of high-directivity antennas in THz systems is able to provide higher antenna gains with small transceiver antenna beamwidths to serve a longer transmission distance, it causes additional problems, e.g., the pointing errors and loss of connection, even for simple shakes or rotations resulted from user equipment mobility [23]. Moreover, if there is neither enough information about NLOS channels between the transmitter and the receiver nor enough information about the reflected paths utilized at particular time, the omnidirectional antenna will be a better choice than the directional antenna [24], which results in the co-channel interference in the THz band.

Under the same user behavior patterns, the co-channel interference in the THz band is much less than that in the microwave band. However, it should be fully noted that the user behavior patterns are versatile, especially when entering the beyond-5G and 6G era. For example, in the context of the Industrial Internet of Things (IIoT) and vertical sectors supported communications, there is an increasing number of machine nodes in smart factories deployed on a highly dense basis [25], and more and more energy-efficient wireless sensors with limited processing capability are in use for environmental monitoring purposes [26]. In this regard, without appropriate

This work was supported by KAUST Office of Sponsored Research.

J. Ye, S. Dang, B. Shihada and M.-S. Alouini are with Computer, Electrical and Mathematical Science and Engineering Division, King Abdullah University of Science and Technology (KAUST), Thuwal 23955-6900, Kingdom of Saudi Arabia (e-mail: {jia.ye, shuping.dang, basem.shihada, slim.alouini}@kaust.edu.sa).

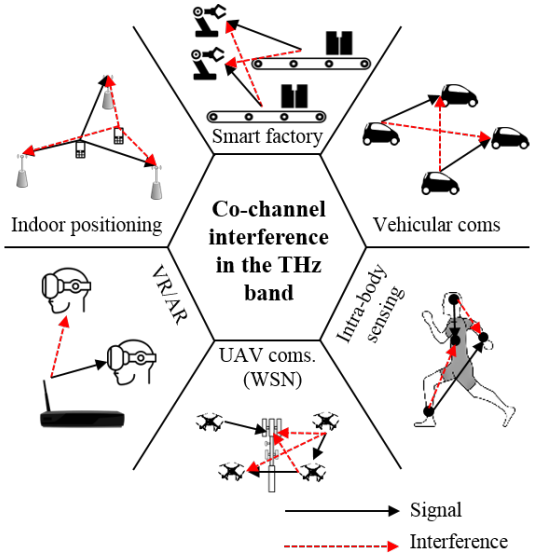

Fig. 1: Emerging scenarios of co-channel interference in the THz band.

spatial arrangement and coordination, the frequency reuse in the THz band can also lead to severe co-channel interference even using directional antennas. The resulted low signal-to-interference-plus-noise ratio (SINR) ultimately degrades signal detection and network reliability [27].

Therefore, because the user behavior patterns were retrieved from classic wireless communications dominated by human users over the microwave spectrum in the past decades, the corresponding co-channel interference models might not be applicable anymore [28]. As a result, co-channel interference in the THz band is worth investigating and becomes even a prominent research topic in recent years [29]. We summarize and pictorially illustrate the emerging scenarios of co-channel interference in the THz band in Fig. 1.

In particular, the studies on the interference in the THz band can be classified into two categories corresponding to the micro-scale and macro-scale THz communication networks. The former is dedicated to the THz enabled nano communications embedded in biological systems/organizations [30], while the latter is mainly associated with the indoor wireless access within ten-meter separation [31]. In [32], the co-channel interference is first analyzed for pulse-based micro-scale THz communication networks, and a channel coding scheme is proposed for co-channel interference mitigation. Following this original study, the information capacity considering multiple co-channel interferers is analyzed for a similar micro-scale scenario in [33], where the aggregate interference is modeled as Gaussian distributed. In [34], the energy-harvesting functionality of intra-body nano sensors is considered in THz intra-body networks, and the co-channel interference is modeled to be a collision event. The link budget planning for the intra-body THz networks is studied based on the constructed aggregate interference model in [35].

The co-channel interference and SINR in the THz band are first analyzed via stochastic geometry in [36], suited for both micro- and macro-scale THz networks. The aggregate interference is also modeled as Gaussian distributed under certain conditions. Shortly after this pioneering study, the THz channel reuse and system optimization issues are discussed in [37] by the authors. Furthermore, the effects of shadowing in the THz band is modeled as a thinning process based on the stochastic geometrical model, and the directional antenna architecture is introduced to alleviate co-channel interference in [38]. In addition, both micro-scale and macro-scale interferers are jointly considered for the co-channel interference modeling in the THz band in [39]. Following the same analytical framework, a comprehensive investigation into the co-channel interference in the THz band is given in [27], where the considered THz network is assumed to be multi-dimensional and interference limited. The mobility of THz transceivers is integrated into the analytical framework for vehicle-to-vehicle (V2V) communication systems in [40], but only the light-of-sight (LoS) and lower-order reflections are taken into account for interference modeling. Also, in [41], the stochastic geometry aided interference model is applied to the virtual reality (VR) application networks with two types of interferers. The stochastic geometry aided interference model is tested and validated through physical experiments for pulse-based THz communication systems in [42].

Although all aforementioned works are insightful and provide a solid basis for predicting the behaviors of the co-channel interference in the THz band, as also pointed out in [27], the stochastic channel impairments, e.g., dynamic shadowing and multi-path fading, have not been fully considered in the co-channel interference model or are incorporated in an oversimplified way. Apart from the node mobility, the THz wireless channel models studied in these works are deterministic, and the non-LoS components over THz wireless channels are to some extent simplified and even ignored. As a consequence, none of the models presented in the aforementioned papers introduces small-scale fading models to synthesize multi-path fading, an important stochastic channel variation mechanism. The latest work incorporating most crucial channel impairments, including spreading loss, molecular absorption loss, shadowing, and multi-path fading in the analysis of THz co-channel interference is reported in [43]. However, the dynamic shadowing phenomenon in this work is again modeled by a blockage probability in a binary manner. Therefore, this model can only provide a qualitative characterization of dynamic shadowing, but can hardly give quantitative measures. Also, because a modified log-normal distribution model is utilized in this paper to model the aggregate interference, the analytical results are not given in a closed form and thereby difficult for further processing.

To capture the peculiarities of THz radios in a comprehensive manner and maintain an adequate equilibrium between fidelity of realistic THz channels and mathematical tractability, we introduce the compound channel model that is originally designed for microwave wireless channels to model the interference in the THz band. The compound channel model has been widely used for modeling microwave wireless channels and is regarded as a general channel model that is capable of efficiently incorporating almost all known deterministic and stochastic channel impairments in the microwave band [44].

The compound channel model is also known as the composite channel model, the Nakagami-Gamma channel model, and the generalized-K channel model, which is originated in [45]. An accurate mapping relation between the classic channel model and the compound channel model is derived in [46]. The compound channel model has also been extensively used to study the aggregate interference in the microwave band and proven to be efficient by both analytical and numerical results presented herein [47]–[52]. As a ripe channel model that has been utilized for more than 15 years, we thereby utilize a tailored compound channel model synthesizing the molecular absorption phenomenon in this paper to study the co-channel interference and SINR in the THz band.

Specifically, the technical contributions of this paper can be summarized as follows:

- We propose a compound interference channel model integrating different features compared to those used in low-frequency bands, including, molecular absorption loss, spreading loss, and dynamical shadowing.
- We approximate the probability density function (PDF) and cumulative distribution function (CDF) of the aggregate co-channel interference in the THz band for a general case with an arbitrary spatial distribution of interferers.
- We analyze the PDF and CDF of the SINR and signal-to-interference ratio (SIR) for a generic case of aggregate co-channel interference by using an approximate interference distribution.
- We specialize the general-purpose interference channel model and analyze the exact and approximate distributions of the SINR and SIR for two special cases: The single-interferer case and the case containing multiple independent and identically distributed (i.i.d.) interferers.
- We provide a series of suggestions obtained from the analytical and numerical results in this paper to help the deployment of dense THz networks with interferers in practice.

To the best of the authors' knowledge, this is the first paper modeling the co-channel interference with all four physical effects (spreading loss, molecular absorption, shadowing, and small-scale fading) and analyzing the SINR/SIR in the THz band by means of a compound channel model.

The rest of the paper is organized as follows. In Section II, we present the system model, including system framework and configurations, compound THz wireless channel model, and noise power. Following the system model constructed, we model the co-channel interference and analyze the SINR and SIR in Section III. We then study several special cases in IV about the SINR and SIR with single-interferer and multiple i.i.d. interferer. Numerical results are presented and discussed in Section V to support the analytical expressions derived in the previous sections and reveal the peculiarities of co-channel interference in the THz band. Finally, we conclude the paper in Section VI.

II. System Model

A. System Framework and Configurations

In this paper, we consider a general multi-user THz wireless communication network, consisting of a targeted transceiver pair and N interferers. The targeted transceiver pair is connected by THz radios over the spectrum $\mathcal{F} = [f_L, f_U] \subseteq [0.1\ \text{THz}, 10\ \text{THz}]$, where f_L and f_U represents the lower and upper limits of the spectrum, respectively, and all transmitting nodes operate over the same spectrum in an underlay manner. Therefore, the available bandwidth for the entire THz wireless communication network is given by $B = f_U - f_L$. The entire bandwidth can be used as a single transmission window or multiple transmission windows depending on the physical separation d_0 between the THz transmitter and receiver.

According to the system framework constructed above, the power spectral density (PSD) of the received signal at the targeted THz receiver, $\forall\ f \in \mathcal{F}$, can be expressed as

$$S_{R_0}(d_0, f) = \tilde{g}_0(d_0, f) G_T(d_0, f) G_{R_0}(d_0, f) S_{T_0}(d_0, f), \quad (1)$$

where $S_{T_0}(d_0, f)$ is the PSD of the transmit signal at the targeted THz transmitter, $G_{T_0}(d_0, f)$ and $G_{R_0}(d_0, f)$ are the transmit and receive antenna gains to model the effects of directional antenna architecture and beamforming techniques, which are unity when omnidirectional antennas are utilized, $\tilde{g}_0(d_0, f)$ is the end-to-end channel power gain, integrating the effects of spreading loss, molecular absorption loss, dynamic shadowing, and multi-path fading. $\tilde{g}_0(d_0, f)$ is associated with the physical characteristics of THz wireless channels and can be regarded as the internal attribute. Note that, we intend to make all above configurations are distance- and frequency-dependent to allow adaptive system optimization, e.g., distance-aware distance-aware bandwidth-adaptive resource allocation [31].

Similarly, the PSD of a single interference generated by the nth interferer at the receiver can be determined by

$$S_{R_n}(d_n, f) = \tilde{g}_n(d_n, f) G_{T_n}(d_n, f) G_{R_n}(d_n, f) S_{T_n}(d_n, f), \quad (2)$$

where $n \in \{1, 2, \cdots, N\}$. Because of the additivity of co-channel interference from multiple interferers, we can have the PSD of the aggregate interference infra:

$$S_I(\mathbf{d}(N), f) = \sum_{n=1}^{N} S_{R_n}(d_n, f), \quad (3)$$

where $\mathbf{d}(N) = [d_1, d_2, \ldots, d_N]^T$.

According to (1) and (3), the signal power and interference power can be written as

$$P_R(d_0) = \int_{\mathcal{F}} S_{R_0}(d_0, f) \mathrm{d}f, \quad (4)$$

and

$$P_I(\mathbf{d}(N)) = \int_{\mathcal{F}} S_I(\mathbf{d}(N), f) \mathrm{d}f. \quad (5)$$

As all terms given above are related to the frequency f and the communication distance d_n, we denote $\tilde{g}_n(d_n, f) = \tilde{g}_n$, $G_{T_n} = G_{T_n}(d_n, f)$,$G_{R_n} = G_{R_n}(d_n, f)$, $S_{T_n} = S_{T_n}(d_n, f)$ for simplicity in the following calculation. Taking the PSD of the transmit signal, the transmit and receive antenna gains as the deterministic values, the received PSD varies with the end-to-end channel power gain $\tilde{g}_0(d_0, f)$. As stated before, the channel gain is determined by several features, which is different from those used in the low-frequency channel.

One of the most important effects is molecular absorption loss, which is caused by high radio frequencies of THz communications and the corresponding wavelengths. It not only brings extra path loss but also leads to a special form of noise. Moreover, the spreading loss related to the transmission frequency and abiding the Friis' transmission law is also an important characteristic of THz communications, which leads to limited transmission coverage compared to low frequencies. The use of the small wavelength of THz radios makes the propagation sensitive to human movement, leading to the dynamic nature of shadowing for THz communications. All these features should all be modeled as stochastic factors in THz communications, which results in a different channel model compared to those used in low-frequency bands. Accordingly, the considered co-channel interference model composed of one targeted THz channel and multiple interference channels are influenced by these unique characteristics, which leads to a more complicated channel model than those used in low-frequency bands.

In the following, we will give the details of the THz wireless channel model and noise model, which are affected by these aforementioned features.

B. Compound THz Wireless Channel Model

Following the compound channel model for microwave channels stated in [46], the PDF of the received PSD $S_{Rn}, n \in \{0, 1, \cdots, N\}$ for THz channels can be similarly expressed as

$$f_{S_{Rn}}(x) = \frac{2b_n^{m_{A_n}}}{\Gamma(m_{\Omega_n})\Gamma(m_{g_n})} x^{\frac{m_{A_n}}{2}-1} K_{m_{M_n}}(2b_n\sqrt{x}), \quad (6)$$

where $m_{g_n} > 0$ is a distance- and frequency-dependent fading figure characterizing the nature of the small-scale fading for a given propagation environment, $m_{\Omega_n} = \frac{1}{\exp(\sigma_n^2)-1}$, $\sigma_n > 0$ is the shadowing figure that characterizes the severity of shadowing and is related to the material of obstacle, $b_n = \sqrt{\frac{m_{\Omega_n} m_{g_n}}{\Omega_n}}$, $\Omega_n = G_n \frac{\psi_n \exp(\sigma_n^2/2)}{\left(\frac{4\pi d_n f}{c}\right)^{\alpha}}$, $G_n = G_{T_n} G_{R_n} S_{T_n}$, $\psi_n = \exp\left(-k_{A_n}(f) d_n\right)$ characterizes the severity of molecular absorption loss, $k_{A_n}(f)$ is the medium absorption coefficient that is related to the radio frequency, the propagation medium composition, the equivalent medium temperature in Kelvin, and the equivalent medium pressure, c is the light of speed, $\alpha \in [2, 7]$ is the spreading loss exponent depending on terrain, $m_{A_n} = m_{\Omega_n} + m_{g_n}$ and $m_{M_n} = m_{\Omega_n} - m_{g_n}$, $\Gamma(\cdot)$ denotes the gamma function, $K_v(\cdot)$ represents the vth-order modified Bessel function of the second kind. Accordingly, the CDF of the received PSD $S_{Rn}, n \in \{0, 1, \cdots, N\}$ is given by

$$\begin{aligned} F_{S_{Rn}}(x) = {} & C_{n1} x^{m_{g_n}} {}_1F_2\left(m_{g_n}; 1 - m_{M_n}, 1 + m_{g_n}; b_n^2 x\right) \\ & + C_{n2} x^{m_{\Omega_n}} {}_1F_2\left(m_{\Omega_n}; 1 + m_{\Omega_n}, 1 + m_{M_n}; b_n^2 x\right), \end{aligned} \quad (7)$$

where $C_{n1} = \frac{b_n^{2m_{g_n}} \Gamma(m_{M_n})}{\Gamma(m_{\Omega_n})\Gamma(m_{g_n}) m_{g_n}}$, $C_{n2} = \frac{{b_n}^{2m_{\Omega_n}} \Gamma(-m_{M_n})}{\Gamma(m_{\Omega_n})\Gamma(m_{g_n}) m_{\Omega_n}}$, and ${}_1F_2(\cdot;\cdot,\cdot;\cdot)$ represents the hypergeometric function.

C. Noise Model in the THz Band

In this paper, we adopt the noise model discussed in [53] and justified in [36], [38], which is given by

$$N(d_0, \mathbf{d}(N), f) = \sum_{n=0}^{N} N_{A_n}(d_n, f) + N_0, \quad (8)$$

where $N_0 = k_B T$ is the PSD of the background thermal noise in the THz band, $N_{A_n}(d_n, f)$ is the PSD of the molecular absorption noise for n-th transmission link, which is given by

$$N_{A_n}(d_n, f) = G_{T_n} G_{R_n} S_{T_n} \left(\frac{c}{4\pi f d_n}\right)^{\alpha} (1 - \psi_n). \quad (9)$$

This molecular absorption noise model captures the prominent features of the molecular absorption noise and is easy to analyze. The noise model is dependent on transmission distance, radio frequency, and the PSD of the transmit signal. Similarly, we simplify $N_{A_n}(d_n, f)$ as N_{A_n} in the following calculation.

III. Analysis of SINR and SIR

In this section, we derive the distribution of the SINR and SIR for a small and flat fading bandwidth B. However, the computation of such a channel model, which contains the hypergeometric function term, is not straightforward due to the associated numerical instabilities that will require the use of approximations and asymptotic expansions or the numerical inversion of the characteristic function. Therefore, the approximation proposed in [54] by adopting the moment matching method with the gamma distribution is considered for the interference channel model.

A. Statistical Model of Co-Channel Interference

It can be observed that the SINR/SIR is related to the sum of S_{R_n} following the generalized-K distribution. To characterize SINR/SIR, the distribution of the aggregate interference needs to be investigated. However, to the best of the authors' knowledge, there is no closed-form expression for the distribution of the sum of non-independent and identically distributed (n.i.i.d) generalized-K distributed random variables (RVs). It is quite involved even for the i.i.d case due to the difficulties associated with the Whitaker function. In other words, further derivations using the characteristic function approach, such as the PDF of the sum of N generalized-K distributed RVs, are not straightforward. To handle this problem and further study the characteristic of SINR/SIR, we approximate the distribution of the sum of generalized-K distributed RVs in closed-form expression through the well-known moment matching method [54]. Specifically, the gamma distribution with an adjustable form for the scale and shape parameters is proposed to approximate the sum of generalized-K distributed RVs by matching the first two positive moments. Such matching results in involved expressions are simple to handle and accurate for most practical values of multipath fading and shadowing parameters. Its computational superiority is also verified in simulation results, which are in tight agreement with the compound THz channel distribution for all cases.

Therefore, the PDF and CDF of the approximated aggregate interference signal are given by

$$f_{S_I}(x) = \frac{\theta_I^{-k_I}}{\Gamma(k_I)} x^{k_I - 1} \exp\left(-\frac{x}{\theta_I}\right), \quad (10)$$

and

$$F_{S_I}(x) = \frac{\gamma\left(k_I, \frac{x}{\theta_I}\right)}{\Gamma(k_I)}, \tag{11}$$

where $\gamma(\cdots,\cdots)$ represents the lower incomplete gamma function, θ_I and k_I are given by

$$\theta_I = \frac{\sum_{n=1}^{N}\left[\mathrm{AF}_n - \epsilon_n\right] G_n^2 \Omega_n^2}{\sum_{n=1}^{N} G_n \Omega_n}, \tag{12}$$

and

$$k_I = \frac{\left(\sum_{n=1}^{N} G_n \Omega_n\right)^2}{\sum_{n=1}^{N}\left[\mathrm{AF}_n - \epsilon_n\right] G_n^2 \Omega_n^2}, \tag{13}$$

where $\mathrm{AF}_n = \frac{1}{m_{g_n}} + \frac{1}{m_{\Omega_n}} + \frac{1}{m_{g_n} m_{\Omega_n}}$, $\forall\, n \in \{0, 1, \cdots, N\}$, ϵ_n is a adjustment factor satisfying $-\mathrm{AF}_n < \epsilon_n < \mathrm{AF}_n$. The introduced adjustment factor here is to ensure that the approximate gamma distribution matches the proposed THz channel model in an accurate manner. Specifically, the shape and scale parameters of the gamma distribution are obtained through the moment matching method with only the first and second moments, which results in a good fit around the mean but poor approximation in the lower and upper tail regions. Since the involved higher-order moments are difficult or even impossible to be derived, an adjustment factor is introduced to adjust the shape and scale parameters to tackle this problem. It should be noted that AF_n added with the scale parameter of the approximate gamma distribution should not exceed the amount of fading of the original distribution, which indicates that the value of the adjustment factors $\{\epsilon_n\}_{n=1}^{N}$ should satisfy the constraint mentioned above.

The optimal value of $\{\epsilon_n\}_{n=1}^{N}$ can be estimated through maximum likelihood estimation (MLE) method, which has been proven to be feasible for most parameter estimation problems [55]. Based on a specific space-frequency state (d, f) and S measured samples of independent random realizations of the received PSD, denoted as $\{S_{R_n,s}\}_{s=1}^{S}$, we can employ the MLE method to obtain the optimal $\{\epsilon_n\}_{n=1}^{N}$ for a specific space-frequency state (d, f). The MLE function based on the specific space-frequency state (d, f) and S independent random samples can be written as

$$\ell\left(\{\epsilon_n\}_{n=1}^{N} \mid \{S_{R_n,s}\}_{s=1}^{S}\right) = \log\left(\prod_{s=1}^{S} f_{S_I}\left(S_{R_n,s}; \{\epsilon_n\}_{n=1}^{N}\right)\right), \tag{14}$$

where $\log(\cdot)$ represents the natural logarithmic function and is introduced to facilitate the processing and manipulation of the MLE function. As a result, we can estimate the optimal $\{\epsilon_n\}_{n=1}^{N}$ according to the following MLE optimization problem:

$$\begin{aligned}\{\epsilon_n\}_{n=1}^{N} = \underset{\{\epsilon_n\}_{n=1}^{N}}{\arg\max} &\left\{\sum_{s=1}^{S} \log\left(f_{S_I}\left(S_{R_n,s}; \{\epsilon_n\}_{n=1}^{N}\right)\right)\right\} \\ \text{s.t.,}\ &-\mathrm{AF}_n < \epsilon_n < \mathrm{AF}_n.\end{aligned} \tag{15}$$

It can be observed from (12) and (13) that the shape and scale parameters θ_I and k_I are related to $\{\epsilon_n\}_{n=1}^{N}$. To ease the optimization process, we re-expressed the common terms in θ_I and k_I as $\Delta = \sum_{n=1}^{N}\left[\mathrm{AF}_n - \epsilon_n\right] G_n^2 \Omega_n^2$ and $\Theta = \sum_{n=1}^{N} G_n \Omega_n$. Accordingly, the objective function in (15) can be further re-expressed as

$$\begin{aligned}\Delta = \underset{\Delta}{\arg\max} &\left\{\sum_{s=1}^{S} \log\left(f_{S_I}\left(S_{R_n,s}; \Delta\right)\right)\right\} \\ \text{s.t.,}\ &0 < \Delta < \sum_{n=1}^{N} 2\mathrm{AF}_n G_n^2 \Omega_n^2,\end{aligned} \tag{16}$$

where the objective function can be explicitly rewritten and simplified to be

$$\begin{aligned}&\sum_{s=1}^{S} \log\left(f_{S_I}\left(S_{R_n,s}; \Delta\right)\right) \\ &= \sum_{s=1}^{S} \log\left(\frac{\left(\frac{\Delta}{\Theta}\right)^{-\frac{\Theta^2}{\Delta}}}{\Gamma(\frac{\Theta^2}{\Delta})} S_{R_n,s}^{\frac{\Theta^2}{\Delta}-1} \exp\left(-\frac{S_{R_n,s}}{\frac{\Delta}{\Theta}}\right)\right) \\ &= -\frac{S\Theta^2}{\Delta}\log\left(\frac{\Delta}{\Theta}\right) - S\log\left(\Gamma(\frac{\Theta^2}{\Delta})\right) \\ &\quad + \left(\frac{\Theta^2}{\Delta} - 1\right)\sum_{s=1}^{S}\log\left(S_{R_n,s}\right) - \frac{\Theta}{\Delta}\sum_{s=1}^{S} S_{R_n,s}.\end{aligned} \tag{17}$$

Since the objective function given in (17) involved with the multiplicative factor $\log\left(\Gamma(\frac{\Theta^2}{\Delta})\right)$, which is hard to handle, we re-represent the optimization variable as $\Delta = \frac{1}{t}$. Accordingly, the objective function can be re-written as

$$\begin{aligned}\sum_{s=1}^{S} \log\left(f_{S_I}\left(S_{R_n,s}; t\right)\right) &= S\Theta^2 t \log(t\Theta) - S\log\left(\Gamma(\Theta^2 t)\right) \\ &+ \left(\Theta^2 t - 1\right)\sum_{s=1}^{S}\log\left(S_{R_n,s}\right) - \Theta t\sum_{s=1}^{S} S_{R_n,s}.\end{aligned} \tag{18}$$

As a result, the second derivative of the re-written objective function can be easily obtained as

$$\frac{\partial^2 \sum_{s=1}^{S} \log\left(f_{S_I}\left(S_{R_n,s}; t\right)\right)}{\partial t^2} = \frac{S\Theta^2}{t} - S\Theta^4 \psi_1\left(\Theta^2 t\right), \tag{19}$$

where $\psi_1(\cdot)$ denotes the Trigamma function, which can be re-represented as

$$\begin{aligned}\psi_1(t) &= \sum_{k=0}^{\infty} \frac{1}{(k+t)^2} \\ &> \sum_{k=0}^{\infty} \frac{1}{(k+t)(k+t+1)} \\ &= \sum_{k=0}^{\infty}\left(\frac{1}{(k+t)} - \frac{1}{(k+t+1)}\right) \\ &= \frac{1}{t} - \lim_{k\to\infty}\frac{1}{(k+t+1)}\end{aligned} \tag{20}$$

Since $\lim_{k\to\infty}\frac{1}{(k+t+1)} = 0$, we can obtain that $\psi_1(t) \geq \frac{1}{t}$. Therefore, we have $\frac{S\Theta^2}{t} - S\Theta^4\psi_1\left(\Theta^2 t\right) = S\Theta^4\left(\frac{1}{\Theta^2 t} - \psi_1\left(\Theta^2 t\right)\right) \leq 0$. In other words, the second

derivative of the objective function is smaller than 0, which indicates its concavity. Also, the constraint can be transferred as $\frac{1}{\sum_{n=1}^{N} 2\mathrm{AF}_n G_n^2 \Omega_n^2} < t$, which is still a concave inequality constraint. In summary, the optimization problem is a concave maximization problem, which can be re-written as

$$\begin{aligned} t = \arg\max_{t} & \left\{ \sum_{s=1}^{S} \log\left(f_{S_I}\left(S_{R_n,s}; t\right)\right) \right\} \\ \text{s.t.,} & \frac{1}{\sum_{n=1}^{N} 2\mathrm{AF}_n G_n^2 \Omega_n^2} < t, \end{aligned} \tag{21}$$

By utilizing the logarithmic barrier method, the problem given in (21) can be approximated as a non-constraint problem, where the objective function is

$$\begin{aligned} \delta\left(t \mid \{S_{R_n,s}\}_{s=1}^{S}\right) &= -\sum_{s=1}^{S} \log\left(f_{S_I}\left(S_{R_n,s}; t\right)\right) \\ &- \tau \left[\log\left(t - \frac{1}{\sum_{n=1}^{N} 2\mathrm{AF}_n G_n^2 \Omega_n^2}\right)\right], \end{aligned} \tag{22}$$

where $\tau > 0$ is a process control parameter, which controls the accuracy of the above approximation. As τ approaches zero, the approximate non-constraint optimization problem becomes an ever-better approximation to the original problem. Therefore, the problem formulated in (21) can be approximated by the following problem:

$$t = \arg\min_{t} \left\{ \delta\left(t \mid \{S_{R_n,s}\}_{s=1}^{S}\right) \right\}. \tag{23}$$

Consequently, the global optimum of the formulated non-constraint convex optimization problem can be easily achieved by existing optimization methods with much reduced computation complexity, such as the gradient descent method [56].

B. Distribution Analysis of SINR

Based on the flat fading assumption, the SINR can be expressed as

$$\begin{aligned} \mathrm{SINR} &= \frac{B S_{R_0}}{B \sum_{n=1}^{N} S_{R_n} + B\left(\sum_{n=0}^{N} N_{A_n}(d_n, f) + N_0\right)} \\ &= \frac{S_{R_0}}{S_I + N_S}. \end{aligned} \tag{24}$$

In the following, we analyze its distribution by adopting the approximated interference distribution.

1) Approximated Distribution Analysis of SINR: Combining the PDF of the approximated aggregate interference PSD given in (10) and the PDF of the target received PSD shown in (6), we can derive the PDF of SINR in integral form as

$$\begin{aligned} f_{SINR}(x) &= \int_{N_S}^{\infty} y f_{S_0}(xy) f_{S_I}(y - N_S)\, \mathrm{d}y \\ &= \int_{N_S}^{\infty} \frac{2 b_0^{m_{A_0}} \theta_I^{-k_I} \exp(\frac{N_S}{\theta_I}) x^{\frac{m_{A_0}}{2}-1}}{\Gamma(m_{\Omega_0})\Gamma(m_{g_0})\Gamma(k_I)} y^{\frac{m_{A_0}}{2}} \\ &\times K_{m_{M_0}}(2b_0\sqrt{xy})(y - N_S)^{k_I - 1} \exp\left(-\frac{y}{\theta_I}\right) \mathrm{d}y. \end{aligned} \tag{25}$$

The expression involving Bessel function is complex, making the simplification of the above integral rather hard. As a solution, we invoke the Chebyshev-Gauss quadrature approximation, which can be given in the form as $\int_{-1}^{1} \frac{f(x)}{\sqrt{1-x^2}} \mathrm{d}x \approx \sum_{i=1}^{W} w f(x_i)$ with $x_i = \cos\left(\frac{2i-1}{2W}\pi\right)$ and the weight $w = \frac{\pi}{W}$. Thus, the PDF of SINR can be approximated as in (26), where $w_I = \frac{\pi}{W_I}$, $\vartheta_i = \cos\left(\frac{2i-1}{2W_I}\pi\right)$.

Even utilizing the Chebyshev-Gauss quadrature approximation, the expression given in (26) can hardly help with the derivation of the CDF of SINR due to the highly complex expressions involved. Therefore, we adopt the distribution of S_{R_0} and S_I shown in (7) and (10) to derive the CDF of SINR as

$$\begin{aligned} F_{SINR}(x) &= \int_{0}^{\infty} F_{S_0}\left(x(y + N_S)\right) f_{S_I}(y)\, \mathrm{d}y \\ &= \int_{N_S}^{\infty} F_{S_0}(xt) f_{S_I}(t - N_S)\, \mathrm{d}t. \end{aligned} \tag{27}$$

Adopting the distribution of S_{R_0} and S_I shown in (7) and (10), the integration is still not solvable, unfortunately. However, we can re-express the hypergeometric function by its series as ${}_1F_2(\alpha_1; \beta_1, \beta_2; z) = \sum_{k=0}^{\infty} \frac{(\alpha_1)_k}{(\beta_1)_k (\beta_2)_k} \frac{z^k}{k!}$, which leads to (28), where $\mathcal{F}_1(u, \nu, \mu, \beta)$ is defined in [57, Eq. 3.383.4.11], which be expressed as

$$\begin{aligned} \mathcal{F}_1(u, \nu, \mu, \beta) &= \beta^{-\frac{\mu+\nu}{2}} u^{\frac{\mu+\nu-2}{2}} \Gamma(\mu) \exp\left(-\frac{\beta u}{2}\right) \\ &\times W_{\frac{\nu-\mu}{2}, \frac{1-\mu-\nu}{2}}(\beta u), \end{aligned} \tag{29}$$

where $W_{\lambda,\nu}(\cdot)$ represents the Whittaker functions.

2) Alternative Approximated SINR Distribution Analysis: Since the derived PDF and CDF of SINR in the above are still complex, we derive a simpler alternative approximated PDF and CDF distribution of SINR in the following. The expression can be further approximated by adopting the approximated PDF and CDF of received signal PSD with the special case with $N = 1$, which can be expressed as

$$f_{S_{R_0}}(x) = \frac{\theta_0^{-k_0}}{\Gamma(k_0)} x^{k_0 - 1} \exp\left(-\frac{x}{\theta_0}\right), \tag{30}$$

and

$$F_{S_{R_0}}(x) = \frac{\gamma\left(k_0, \frac{x}{\theta_0}\right)}{\Gamma(k_0)}, \tag{31}$$

where $\theta_0 = [\mathrm{AF}_0 - \epsilon_0] G_0 \Omega_0$, ϵ_0 is the adjustment factor, satisfying $-\mathrm{AF}_0 < \epsilon_0 < \mathrm{AF}_0$, and $k_0 = \frac{1}{\mathrm{AF}_0}$.

$$
\begin{aligned}
f_{SINR}(x) &= \int_0^{N_S} \frac{2b_0^{m_{A_0}}\theta_I^{-k_I}\exp(\frac{N_S}{\theta_I})x^{\frac{m_{A_0}}{2}-1}}{\Gamma(m_{\Omega_0})\Gamma(m_{g_0})\Gamma(k_I)} t^{-\frac{m_{A_0}}{2}-2} K_{m_{M_0}}\left(2b_0\sqrt{\frac{x}{t}}\right)\left(\frac{1}{t}-N_S\right)^{k_I-1}\exp\left(-\frac{1}{t\theta_I}\right)\mathrm{d}t. \\
&= \int_{-1}^{1} \frac{2^{\frac{m_{A_0}}{2}+2}b_0^{m_{A_0}}\theta_I^{-k_I}\exp(\frac{N_S}{\theta_I})x^{\frac{m_{A_0}}{2}-1}}{\Gamma(m_{\Omega_0})\Gamma(m_{g_0})\Gamma(k_I)N_S^{\frac{m_{A_0}}{2}+1}}(t+1)^{-\frac{m_{A_0}}{2}-2} K_{m_{M_0}}\left(2b_0\sqrt{\frac{2x}{N_S(t+1)}}\right) \\
&\quad\times\left(\frac{2}{N_S(t+1)}-N_S\right)^{k_I-1}\exp\left(-\frac{2}{N_S(t+1)\theta_I}\right)\mathrm{d}t \\
&= \sum_{i=1}^{W_I} w_I\sqrt{1-\vartheta_i^2}\frac{2^{\frac{m_{A_0}}{2}+2}b_0^{m_{A_0}}\theta_I^{-k_I}\exp(\frac{N_S}{\theta_I})x^{\frac{m_{A_0}}{2}-1}}{\Gamma(m_{\Omega_0})\Gamma(m_{g_0})\Gamma(k_I)N_S^{\frac{m_{A_0}}{2}+1}}(\vartheta_i+1)^{-\frac{m_{A_0}}{2}-2} K_{m_{M_0}}\left(2b_0\sqrt{\frac{2x}{N_S(\vartheta_i+1)}}\right) \\
&\quad\times\left(\frac{2}{N_S(\vartheta_i+1)}-N_S\right)^{k_I-1}\exp\left(-\frac{2}{N_S(\vartheta_i+1)\theta_I}\right)
\end{aligned} \tag{26}
$$

$$
\begin{aligned}
F_{SINR}(x) &= \sum_{k=0}^{\infty}\frac{C_{01}(m_{g_0})_k b_0^{2k}\theta_I^{-k_I}\exp(\frac{N_S}{\theta_I})x^{m_{g_0}+k}}{(1-m_{M_0})_k(1+m_{g_0})_k k!\Gamma(k_I)}\int_{N_S}^{\infty} t^{k+m_{g_0}}(t-N_S)^{k_I-1}\exp\left(-\frac{t}{\theta_I}\right)\mathrm{d}t \\
&\quad+\sum_{k=0}^{\infty}\frac{C_{02}(m_{\Omega_0})_k b_0^{2k}\theta_I^{-k_I}\exp\left(\frac{N_S}{\theta_I}\right)x^{k+m_{\Omega_0}}}{(1+m_{\Omega_0})_k(1+m_{M_0})_k k!\Gamma(k_I)}\int_{N_S}^{\infty} t^{k+m_{\Omega_0}}(t-N_S)^{k_I-1}\exp\left(-\frac{t}{\theta_I}\right)\mathrm{d}t \\
&= \sum_{k=0}^{\infty}\frac{C_{01}(m_{g_0})_k b_0^{2k}\theta_I^{-k_I}\exp(\frac{N_S}{\theta_I})x^{m_{g_0}+k}}{(1-m_{M_0})_k(1+m_{g_0})_k k!\Gamma(k_I)}\mathcal{F}_1\left(N_S,k+m_{g_0}+1,k_I,\frac{1}{\theta_I}\right) \\
&\quad+\sum_{k=0}^{\infty}\frac{C_{01}(m_{g_0})_k b_0^{2k}\theta_I^{-k_I}\exp(\frac{N_S}{\theta_I})x^{m_{g_0}+k}}{(1-m_{M_0})_k(1+m_{g_0})_k k!\Gamma(k_I)}\mathcal{F}_1\left(N_S,k+m_{\Omega_0}+1,k_I,\frac{1}{\theta_I}\right)
\end{aligned} \tag{28}
$$

In this case, the PDF distribution of SINR can be calculated as

$$
\begin{aligned}
f_{SINR}(x) &= \int_{N_S}^{\infty} y f_{S_0}(xy) f_{S_I}(y-N_S)\,\mathrm{d}y \\
&= \int_{N_S}^{\infty}\frac{\theta_0^{-k_0}\theta_I^{-k_I}}{\Gamma(k_0)\Gamma(k_I)}\exp(\frac{N_S}{\theta_I})x^{k_0-1} \\
&\quad\times y^{k_0}\exp(-\frac{xy}{\theta_0})(y-N_S)^{k_I-1}\exp(-\frac{y}{\theta_I})\mathrm{d}y \\
&= \frac{\theta_0^{-k_0}\theta_I^{-k_I}}{\Gamma(k_0)}\exp(\frac{N_S}{\theta_I})N_S^{\frac{k_I+k_0-1}{2}}x^{k_0-1} \\
&\quad\times\left(\frac{1}{\theta_I}+\frac{x}{\theta_0}\right)^{-\frac{k_I+k_0+1}{2}}\exp\left(-\frac{\left(\frac{1}{\theta_I}+\frac{x}{\theta_0}\right)N_S}{2}\right) \\
&\quad\times W_{\frac{k_0+1-k_I}{2},\frac{-k_I-k_0}{2}}\left(\left(\frac{1}{\theta_I}+\frac{x}{\theta_0}\right)N_S\right).
\end{aligned} \tag{32}
$$

Similarly, we can derive an alternative approximated CDF of SINR as

$$
\begin{aligned}
F_{SINR}(x) &= \int_0^{\infty} F_{S_0}(x(y+N_S))f_{S_I}(y)\,\mathrm{d}y \\
&= \int_{N_S}^{\infty} F_{S_0}(xt)f_{S_I}(t-N_S)\,\mathrm{d}t \\
&= \int_{N_S}^{\infty} C_I\exp\left(-\frac{t}{\theta_I}\right)(t-N_S)^{k_I-1}\gamma\left(k_0,\frac{xt}{\theta_0}\right)\mathrm{d}t,
\end{aligned} \tag{33}
$$

where $C_I = \frac{\theta_I^{-k_I}}{\Gamma(k_0)\Gamma(k_I)}\exp\left(\frac{N_S}{\theta_I}\right)$. However, this integral is still not solvable. To solve this integral, the lower incomplete gamma function can be re-expressed by series as $\gamma(\alpha,x) = \sum_{n=0}^{\infty}\frac{(-1)^n x^{\alpha+n}}{n!(\alpha+n)}$, which leads to (34). In this way, the integral can be solved with the help of (29).

C. Distribution Analysis of SIR

For highly spectrally efficient interference-limited scenarios where noise becomes negligible compared to the co-channel interference, we study the SIR, instead. Based on the flat fading assumption in the previous section, the SIR can be written as

$$
\text{SIR} = S_{R_0}/S_I. \tag{35}
$$

1) Approximated Distribution Analysis of SIR: Based on the signal spectral distribution shown in (6) and (10), the PDF

$$F_{SINR}(x) = \sum_{n=0}^{\infty} \frac{C_I(-1)^n x^{k_0+n}}{\theta_0^{k_0+n} n!(k_0+n)} \int_{N_S}^{\infty} t^{k_0+n} (t-N_S)^{k_I-1} \exp\left(-\frac{t}{\theta_I}\right) \mathrm{d}t$$
$$= \sum_{n=0}^{\infty} \frac{C_I(-1)^n x^{k_0+n}}{\theta_0^{k_0+n} n!(k_0+n)} \mathcal{F}_1\left(N_S, k_0+n+1, k_I, \frac{1}{\theta_I}\right) \tag{34}$$

of SIR can be derived in a similar manner as

$$f_{SIR}(x) = \int_0^{\infty} y f_{S_0}(xy) f_{S_I}(y)\,\mathrm{d}y$$
$$= \int_0^{\infty} \frac{2b_0^{m_{A_0}} \theta_I^{-k_I}}{\Gamma(m_{\Omega_0})\Gamma(m_{g_0})\Gamma(k_I)} x^{\frac{m_{A_0}}{2}-1} \times y^{\frac{m_{A_0}}{2}+k_I-1} K_{m_{M_0}}(2b_0\sqrt{xy}) \exp\left(-\frac{y}{\theta_I}\right)\mathrm{d}y$$
$$= \frac{b_0^{m_{A_0}-1}\theta_I^{\frac{m_{A_0}}{2}-\frac{1}{2}}\Gamma(m_{\Omega_0}+k_I)\Gamma(m_{g_0}+k_I)}{\Gamma(m_{\Omega_0})\Gamma(m_{g_0})\Gamma(k_I)} \times x^{\frac{m_{A_0}}{2}-\frac{3}{2}} \exp\left(\frac{b_0^2\theta_I x}{2}\right) W_{-\left(\frac{m_{A_0}}{2}+k_I-\frac{1}{2}\right),\frac{m_{M_0}}{2}}\left(b_0^2\theta_I x\right). \tag{36}$$

And ditto the CDF of SIR can be determined in (37) by adopting the distribution of S_{Rn} and S_I shown in (7) and (10). Again, the second equation is obtained by adopting [57, Eq. 7.525.9].

2) Alternative Approximated SIR Distribution Analysis: Similarly, by taking advantage of the approximated PDF of S_{R_0}, the PDF of SIR can be calculated as

$$f_{SIR}(x) = \int_0^{\infty} y f_{S_0}(xy) f_{S_I}(y)\,\mathrm{d}y$$
$$= \int_0^{\infty} \frac{\theta_0^{-k_0}\theta_I^{-k_I} x^{k_0-1}}{\Gamma(k_0)\Gamma(k_I)} \exp\left(-\frac{xy}{\theta_0}\right) y^{k_0+k_I-1} \exp\left(-\frac{y}{\theta_I}\right)\mathrm{d}y$$
$$= \frac{\theta_0^{-k_0}\theta_I^{-k_I}}{\Gamma(k_0)\Gamma(k_I)}\Gamma(k_0+k_I)x^{k_0-1}\left(\frac{x}{\theta_0}+\frac{1}{\theta_I}\right)^{-k_0-k_I}. \tag{38}$$

Following this approximation, the CDF of SIR can be determined as

$$F_{SIR}(x) = \int_0^{\infty} C_N \exp\left(-\frac{y}{\theta_I}\right) y^{k_I-1}\gamma\left(k_0, \frac{xy}{\theta_0}\right)\mathrm{d}y, \tag{39}$$

where $C_N = \frac{\theta_I^{-k_I}}{\Gamma(k_I)\Gamma(k_0)}$. By adopting [57, Eq. 6.455.2], we can finally obtain the approximate expression in closed form as

$$F_{SIR}(x) = \frac{C_N x^{k_0}\Gamma(k_I+k_0)}{\theta_0^{k_0} k_I (\frac{x}{\theta_0}+\frac{1}{\theta_I})^{k_I+k_0}} \times {}_2F_1\left(1, k_I+k_0; k_0+1; \frac{x\theta_I}{x\theta_I+\theta_0}\right). \tag{40}$$

IV. Studies on Special Cases

To illustrate the usefulness of the analytical results given in the last section, we specialize the general derivations in this section and study the co-channel interference for two special cases. The distributions of SINR and SIR on these two special scenarios with only a single interferer and multiple i.i.d. interferers are investigated and discussed.

A. Single-Interferer Case

For the single-interferer case, we discuss its SINR and SIR distribution separately in the following paragraphs.

1) Distribution Analysis of SINR: For the simplest case with only a single interferer, the distribution of the exact SINR is still hard to calculate due to the involved hypergeometric functions and modified Bessel function. As an alternative solution, we adopt the Chebyshev-Gauss quadrature approximation and calculated the PDF of SINR in (41), where $w_I = \frac{\pi}{W_I}$, $\vartheta_i = \cos\left(\frac{2i-1}{2W_I}\pi\right)$. By the relation between PDF and CDF and (41), the CDF of the SINR in the single interferer case can be calculated in the same way in (42), where $w_F = \frac{\pi}{W_F}$, $\nu_i = \cos\left(\frac{2i-1}{2W_F}\pi\right)$.

2) Distribution Analysis of SIR: The noise term can also be ignored when the interference generated by the single interferer plays a dominant role. Therefore, the PDF and CDF SIR for the single-interferer case can be derived as in (43) and (44), respectively, where the third equation in (43) is solved by [57, Eq. 6.576.4], $C_3 = \frac{C_{01}4b_1^{m_{A_1}}}{\Gamma(m_{\Omega_1})\Gamma(m_{g_1})}$, $C_4 = \frac{C_{02}4b_1^{m_{A_1}}}{\Gamma(m_{\Omega_1})\Gamma(m_{g_1})}$, $C_5 = m_{A_1}+2m_{g_0}$, $C_6 = m_{A_1}+2m_{\Omega_0}$, $\mathcal{F}_2(\sigma,\lambda,a_1,b_1,b_2,\nu,y)$ is defined in [57, Eq. 7.542.4] as

$$\mathcal{F}_2(\sigma,\lambda,a_1,b_1,b_2,\nu,y) = \int_0^{\infty} x^{\sigma-1}{}_1F_2\left(a_1; b_1, b_2; -\lambda x^2\right) K_\nu(xy)\mathrm{d}x$$
$$= 2^{\sigma-2}y^{-\sigma}\Gamma\left(\frac{\sigma+\nu}{2}\right)\Gamma\left(\frac{\sigma-\nu}{2}\right) \times {}_3F_2\left(a_1, \frac{\sigma+\nu}{2}, \frac{\sigma-\nu}{2}; b_1, b_2; \frac{4\lambda}{y^2}\right), \tag{45}$$

where ${}_3F_2(\cdot,\cdot,\cdot;\cdot,\cdot;\cdot)$ represents the hypergeometric function.

3) Approximated Distribution Analysis of SINR and SIR: Moreover, we can also obtain the approximated SINR and SIR through (26), (28), (36) and (37) by setting $N=1$, $\theta_I = [\mathrm{AF}_1 - \epsilon_1]\,G_1\Omega_1$, and $k_I = \frac{1}{[\mathrm{AF}_1-\epsilon_1]}$.

B. Case with Multiple i.i.d. Interferers

In this subsection, we study the SINR and SNR under the setting that there exist N mutually independent interferes with statistically identical setups. This assumption is adequate for several kinds of wireless systems, e.g., cooperative communications assisted by clustered relays, multiple-input and multiple-output (MIMO) interferers with closely spaced

$$
\begin{aligned}
F_{SIR}(x) &= \int_0^{\infty} F_{S_0}(xy) f_{S_I}(y)\,\mathrm{d}y \\
&= \int_0^{\infty} \frac{C_{01}\theta_I^{-k_I} x^{m_{g_0}}}{\Gamma(k_I)} y^{m_{g_0}+k_I-1} \exp\left(-\frac{y}{\theta_I}\right) {}_1F_2\left(m_{g_0}; 1-m_{M_0}, 1+m_{g_0}, b_0^2 xy\right)\mathrm{d}y \\
&\quad + \int_0^{\infty} \frac{C_{02}\theta_I^{-k_I} x^{m_{\Omega_0}}}{\Gamma(k_I)} y^{m_{\Omega_0}+k_I-1} \exp\left(-\frac{y}{\theta_I}\right) {}_1F_2\left(m_{\Omega_0}; 1+m_{\Omega_0}, 1+m_{M_0}; b_0^2 xy\right)\mathrm{d}y \\
&= \frac{C_{01}\theta_I^{-k_I}}{\Gamma(k_I)}\Gamma(m_{g_0}+k_I)\theta_I^{m_{g_0}+k_I} x^{m_{g_0}} {}_2F_2\left(m_{g_0}, m_{g_0}+k_I; 1-m_{M_0}, 1+m_{g_0}; b_0^2 x\theta_I\right) \\
&\quad + \frac{C_{02}\theta_I^{-k_I}}{\Gamma(k_I)}\Gamma(m_{\Omega_0}+k_I)\theta_I^{m_{\Omega_0}+k_I} x^{m_{\Omega_0}} {}_2F_2\left(m_{\Omega_0}, m_{\Omega_0}+k_I; 1+m_{\Omega_0}, 1+m_{M_0}; b_0^2 x\theta_I\right)
\end{aligned} \tag{37}
$$

$$
\begin{aligned}
f_{SINR}(x) &= \int_{N_S}^{\infty} y f_{S_0}(xy)\, f_{S_I}(y-N_S)\,\mathrm{d}y \\
&= \int_{N_S}^{\infty} \frac{4 b_0^{m_{A_0}} b_1^{m_{A_1}}}{\Gamma(m_{\Omega_0})\Gamma(m_{g_0})\Gamma(m_{\Omega_1})\Gamma(m_{g_1})} x^{\frac{m_{A_0}}{2}-1} y^{\frac{m_{A_0}}{2}} (y-N_S)^{\frac{m_{A_1}}{2}-1} K_{m_{M_0}}(2b_0\sqrt{xy}) K_{m_{M_1}}(2b_1\sqrt{y-N_S})\mathrm{d}y \\
&= \sum_{i=1}^{W_S} w_S \sqrt{1-\mu_i^2} \frac{2^{\frac{m_{A_0}}{2}+3} b_0^{m_{A_0}} b_1^{m_{A_1}} x^{\frac{m_{A_0}}{2}-1}}{\Gamma(m_{\Omega_0})\Gamma(m_{g_0})\Gamma(m_{\Omega_1})\Gamma(m_{g_1}) N_S^{\frac{m_{A_0}}{2}+1}} \left(\frac{2}{N_S(\mu_i+1)} - N_S\right)^{\frac{m_{A_1}}{2}-1} \\
&\quad \times (\mu_i+1)^{-\frac{m_{A_0}}{2}-2} K_{m_{M_0}}\left(2b_0\sqrt{\frac{2x}{N_S(\mu_i+1)}}\right) K_{m_{M_1}}\left(2b_1\sqrt{\frac{2}{N_S(\mu_i+1)} - N_S}\right)
\end{aligned} \tag{41}
$$

$$
\begin{aligned}
F_{SINR}(x) &= \int_{N_S}^{\infty} F_{S_0}(xt) f_{S_1}(t-N_S)\,\mathrm{d}t \\
&= \int_{N_S}^{\infty} C_{01} x^{m_{g_0}} t^{m_{g_0}} {}_1F_2\left(m_{g_0}; 1-m_{M_0}, 1+m_{g_0}, b_0^2 xt\right) \frac{2 b_1^{m_{A_1}}}{\Gamma(m_{\Omega_1})\Gamma(m_{g_1})} (t-N_S)^{\frac{m_{A_1}}{2}-1} K_{m_{M_1}}(2b_1\sqrt{t-N_S})\mathrm{d}t \\
&\quad + \int_{N_S}^{\infty} C_{02} x^{m_{\Omega_0}} t^{m_{\Omega_0}} {}_1F_2\left(m_{\Omega_0}; 1+m_{\Omega_0}, 1+m_{M_0}; b_0^2 xt\right) \frac{2 b_1^{m_{A_1}}}{\Gamma(m_{\Omega_1})\Gamma(m_{g_1})} (t-N_S)^{\frac{m_{A_1}}{2}-1} K_{m_{M_1}}(2b_1\sqrt{t-N_S})\mathrm{d}t \\
&= \sum_{i=1}^{W_F} w_F \sqrt{1-\nu_i^2} \frac{2^{m_{g_0}+2} C_{01} b_1^{m_{A_1}} x^{m_{g_0}}}{\Gamma(m_{\Omega_1})\Gamma(m_{g_1}) N_S^{m_{g_0}+1}} {}_1F_2\left(m_{g_0}; 1-m_{M_0}, 1+m_{g_0}, \frac{2b_0^2 x}{N_S(\nu_i+1)}\right) \\
&\quad \times (\nu_i+1)^{-m_{g_0}-2} \left(\frac{2-N_S^2(\nu_i+1)}{N_S(\nu_i+1)}\right)^{\frac{m_{A_1}}{2}-1} K_{m_{M_1}}\left(2b_1\sqrt{\frac{2-N_S^2(\nu_i+1)}{N_S(\nu_i+1)}}\right) \\
&\quad + \sum_{i=1}^{W_F} w_F \sqrt{1-\nu_i^2} \frac{2^{m_{\Omega_0}+2} C_{02} b_1^{m_{A_1}} x^{m_{\Omega_0}}}{\Gamma(m_{\Omega_1})\Gamma(m_{g_1}) N_S^{m_{\Omega_0}+1}} {}_1F_2\left(m_{\Omega_0}; 1+m_{\Omega_0}, 1+m_{M_0}; \frac{2b_0^2 x}{N_S(\nu_i+1)}\right) \\
&\quad \times (\nu_i+1)^{-m_{\Omega_0}-2} \left(\frac{2-N_S^2(\nu_i+1)}{N_S(\nu_i+1)}\right)^{\frac{m_{A_1}}{2}-1} K_{m_{M_1}}\left(2b_1\sqrt{\frac{2-N_S^2(\nu_i+1)}{N_S(\nu_i+1)}}\right)
\end{aligned} \tag{42}
$$

$$
\begin{aligned}
f_{SIR}(x) &= \int_0^\infty y f_{S_0}(xy) f_{S_1}(y)\,\mathrm{d}y \\
&= \int_0^\infty \frac{4 b_0^{m_{A_0}} b_1^{m_{A_1}}}{\Gamma(m_{\Omega_0})\Gamma(m_{g_0})\Gamma(m_{\Omega_1})\Gamma(m_{g_1})} x^{\frac{m_{A_0}}{2}-1} y^{\frac{m_{A_0}}{2}+\frac{m_{A_1}}{2}-1} K_{m_{M_0}}(2b_0\sqrt{xy}) K_{m_{M_1}}(2b_1\sqrt{y})\mathrm{d}y \\
&= \int_0^\infty \frac{8 b_0^{m_{A_0}} b_1^{m_{A_1}}}{\Gamma(m_{\Omega_0})\Gamma(m_{g_0})\Gamma(m_{\Omega_1})\Gamma(m_{g_1})} x^{\frac{m_{A_0}}{2}-1} t^{m_{A_0}+m_{A_1}-1} K_{m_{M_0}}(2b_0\sqrt{x}t) K_{m_{M_1}}(2b_1 t)\mathrm{d}t \\
&= \frac{2^{m_{\Omega_1}} b_0^{-m_{\Omega_1}} b_1^{2m_{\Omega_1}} \Gamma(m_{\Omega_0}+m_{\Omega_1})\Gamma(m_{g_0}+m_{\Omega_1})}{\Gamma(m_{\Omega_0})\Gamma(m_{g_0})\Gamma(m_{\Omega_1})\Gamma(m_{g_1})\Gamma(m_{A_0}+m_{A_1})} \Gamma(m_{\Omega_0}+m_{g_1})\Gamma(m_{g_0}+m_{g_1}) x^{-m_{\Omega_1}-1} \\
&\quad \times F\left(m_{\Omega_0}+m_{\Omega_1}, m_{g_0}+m_{\Omega_1}; m_{A_0}+m_{A_1}; 1-\frac{b_1^2}{b_0^2 x}\right)
\end{aligned} \tag{43}
$$

$$
\begin{aligned}
F_{SIR}(x) &= \int_0^\infty F_{S_0}(xy) f_{\tilde{g}_1}(y)\,\mathrm{d}y \\
&= \int_0^\infty \frac{C_{01} x^{m_{g_0}} 2 b_1^{m_{A_1}}}{\Gamma(m_{\Omega_1})\Gamma(m_{g_1})} y^{\frac{m_{A_1}}{2}+m_{g_0}-1} K_{m_{M_1}}(2b_1\sqrt{y})\,{}_1F_2\left(m_{g_0}; 1-m_{M_0}, 1+m_{g_0}, b_0^2 xy\right)\mathrm{d}y \\
&\quad + \int_0^\infty \frac{C_{02} x^{m_{\Omega_0}} 2 b_1^{m_{A_1}}}{\Gamma(m_{\Omega_1})\Gamma(m_{g_1})} y^{\frac{m_{A_1}}{2}+m_{\Omega_0}-1} K_{m_{M_1}}(2b_1\sqrt{y})\,{}_1F_2\left(m_{\Omega_0}; 1+m_{\Omega_0}, 1+m_{M_0}; b_0^2 xy\right)\mathrm{d}y \\
&= \int_0^\infty \frac{C_{01} x^{m_{g_0}} 4 b_1^{m_{A_1}}}{\Gamma(m_{\Omega_1})\Gamma(m_{g_1})} y^{m_{A_1}+2m_{g_0}-1} K_{m_{M_1}}(2b_1 t)\,{}_1F_2\left(m_{g_0}; 1-m_{M_0}, 1+m_{g_0}, b_0^2 x t^2\right)\mathrm{d}t \\
&\quad + \int_0^\infty \frac{C_{02} x^{m_{\Omega_0}} 4 b_1^{m_{A_1}}}{\Gamma(m_{\Omega_1})\Gamma(m_{g_1})} y^{m_{A_1}+2m_{\Omega_0}-1} K_{m_{M_1}}(2b_1 t)\,{}_1F_2\left(m_{\Omega_0}; 1+m_{\Omega_0}, 1+m_{M_0}; b_0^2 x t^2\right)\mathrm{d}t \\
&= C_3 x^{m_{g_0}} \mathcal{F}_2\left(C_5, -b_0^2 x, m_{g_0}, 1-m_{M_0}, 1+m_{g_0}, m_{M_1}, 2b_1\right) + C_4 x^{m_{\Omega_0}} \mathcal{F}_2\left(C_6, -b_0^2 x, m_{\Omega_0}, 1+m_{\Omega_0}, 1+m_{M_0}, m_{M_1}, 2b_1\right)
\end{aligned} \tag{44}
$$

antennas [58], [59]. Based on the proposed compound THz wireless channel model, the PSD of the received signal S_{R_n} can be rewritten as $S_{R_n} = Z_n^2 \tilde{\Omega}_n$, where $Z_n \sim N\left(m_{g_n}, \tilde{\Omega}_n\right)$ and $\tilde{\Omega}_n \sim G(m_{\Omega_n}, \Omega_n)$. By assuming i.i.d. small-scale fading and i.i.d. shadowing processes, we can have $m_{g_n} = m_g$, $\Omega_n = \Omega$, and $m_{\Omega_n} = m_\Omega$, $\forall\ n \in \{1, 2, \ldots, N\}$. Moreover, the multiple interferers can be further characterized by i.i.d. small-scale fading with an identical shadowing factor, which results in $m_{g_n} = m_g$ and $\tilde{\Omega}_n = \tilde{\Omega}$. This manipulation has been utilized and justified in [60], which is quite useful for the derivations of the upper and lower bounds on the system performance by placing all interferers at the best and worst location in terms of the interference level.

1) Non-identical Shadowing Factor: Assuming that all interferers follow the i.i.d. small-scale fading and i.i.d. shadowing processes with $m_{g_n} = m_g$, $\Omega_n = \Omega$, and $m_{\Omega_n} = m_\Omega$, the PDF of the sum of interfering PSDs can be approximated as [61]

$$
f_{S_I}(x) = \frac{2\bar{b}^{\bar{m}_A}}{\Gamma(\bar{m}_g)\Gamma(\bar{m}_\Omega)} x^{\frac{\bar{m}_A-2}{2}} K_{\bar{m}_M}\left(2\bar{b}\sqrt{x}\right), \tag{46}
$$

where $\bar{m}_g = N m_g$, $\bar{m}_\Omega = N m_\Omega + \varepsilon$, $\varepsilon = (N-1)\frac{-0.127-0.95 m_\Omega - 0.0058 m_g}{1+0.00124 m_\Omega + 0.98 m_g}$, $\bar{b} = \sqrt{\frac{\bar{m}_\Omega \bar{m}_g}{\bar{\Omega}}}$, $\bar{\Omega} = N\Omega$, $\bar{m}_A = \bar{m}_\Omega + \bar{m}_g$, and $\bar{m}_M = \bar{m}_\Omega - \bar{m}_g$.

Since the approximated PDF of the sum of multiple i.i.d. interference shares the same form of the interference from a single interferer, the PDFs and CDFs of SINR and SIR can be obtained by replacing $m_{\Omega 1}$, m_{g1}, m_{A1}, and b_1 with $\bar{m}_\Omega$, $\bar{m}_g$, $\bar{m}_A$, and $\bar{b}$. As the derivations are similar to the those presented above, we omit the detailed derivation here for brevity. In addition, the approximated expression can be also obtained by our previous results by setting $\theta_I = (\mathrm{AF} - \epsilon) G\Omega$ and $k_I = \frac{N}{\mathrm{AF}-\epsilon}$, where $\mathrm{AF} = \frac{1}{m_g} + \frac{1}{m_\Omega} + \frac{1}{m_g m_\Omega}$.

2) Identical Shadowing Factor: The identical shadowing factor assumption is useful for modeling several wireless communication systems. For example, MIMO interfering signals coming from collocated antennas are subject to the same shadowing process and constrained to be equidistant from the desired user [62]. Under the assumption of the identical shadowing factor, we adopt the PDF of the aggregate interference term given in [48] as

$$
f_{S_I}(x) = \frac{2 b^{m_A}}{\Gamma(N m_g)\Gamma(m_\Omega)} x^{\frac{m_A-2}{2}} K_{m_\Omega - N m_g}\left(2b\sqrt{x}\right), \tag{47}
$$

where $b = \sqrt{\frac{m_\Omega m_g}{\Omega}}$ and $m_A = m_\Omega + N m_g$. Therefore, the PDFs and CDFs of SINR and SIR can be derived through the similar process as for the single-interferer case and can be obtained by replacing $m_{\Omega 1}$, m_{g1}, m_{A1}, and b_1 with m_Ω, $N m_g$, m_A, and b. The derived results given above can provide the insights into the worst and best interference configurations.

V. Numerical Results and Discussion

In this section, we present numerical results generated by Monte Carlo simulations to verify the effectiveness of our SINR and SIR analysis based on the approximate gamma distribution. The interfering nodes are assumed to be distributed around the desired receiver from 0 m to 4 m [27], while the communication distance between the targeted receiver and transmitter is set as $d_0 = 1$ m. Both the targeted signals and the interfering experience the same propagation environment. Following the parameters adopted in [63]–[65], the main parameters in our simulations are set as: $f = 0.3$ THz, $\alpha = 2$, $T = 290$ K, $k_{A_0}(f) = 0.001$ m^{-1}, $\sigma_0 = 0.5$ dB, $m_{g_0} = 6$, $G_{T_0} = G_{R_0} = 20$ dB, $S_{T_0} = 1$, $k_{A_n}(f) = 0.2$ m^{-1}, $\sigma_n = 2$ dB, $m_{g_n} = 3$, $G_{T_n} = G_{R_n} = 1$, $S_{T_n} = 1$, $n \in [1, \cdots, N]$, and $W_I = W_S = W_F = 20$.

A. Channel Approximation

To begin with, we examine the convergence between the approximated gamma distribution and the distribution of the aggregate interference channel with a well-chosen parameter $\{\epsilon_n\}_{n=1}^N$. With different channel parameters, the parameter $\{\epsilon_n\}_{n=1}^N$ is yielded by the MLE method stipulated in (15) with $S = 1000$ random samples. The approximation results for single signals and sum of received signals are shown in Fig. 2 and Fig. 3, respectively. The parameter sets adopted in Fig. 3 for $N = 2, 3, 4$ are denoted as $\mathcal{S}_2$, $\mathcal{S}_3$, $\mathcal{S}_4$ separately, where $\mathcal{S}_2$ is composed by $\{d_n\}_{n=1}^N = 3, 4$ m, $\mathcal{S}_3$ is composed by $\mathcal{S}_2$ and $d_n = 2$ m, $\mathcal{S}_4$ is composed by $\mathcal{S}_3$ and $d_n = 1.5$ m. Observing Fig. 2 and Fig. 3, the approximated gamma distribution and the compound THz channel distribution closely match each other for all cases. As a result of this convergence, the effectiveness of the gamma distribution approximation with a well-chosen ϵ_n is validated, which implies that the gamma distribution can capture the statistical traits of the THz wireless channel with much simpler expressions. Moreover, as can be seen from Fig. 2, the impact of the distance on channel gain decreases as the distance increases.

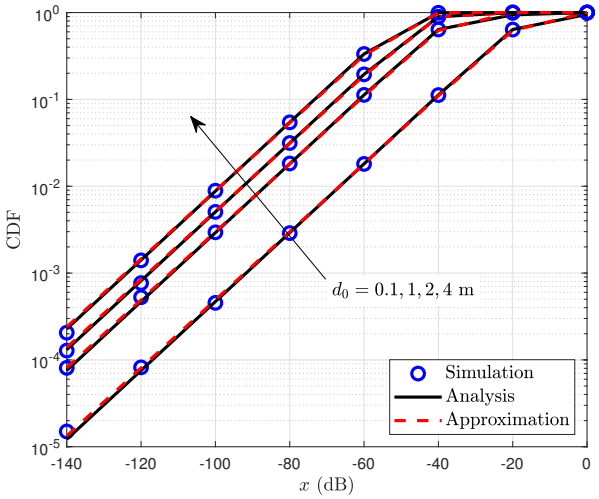

Fig. 2: Comparison between the exact THz channel CDF and the approximate gamma CDF with optimal ϵ_n of a single received PSD.

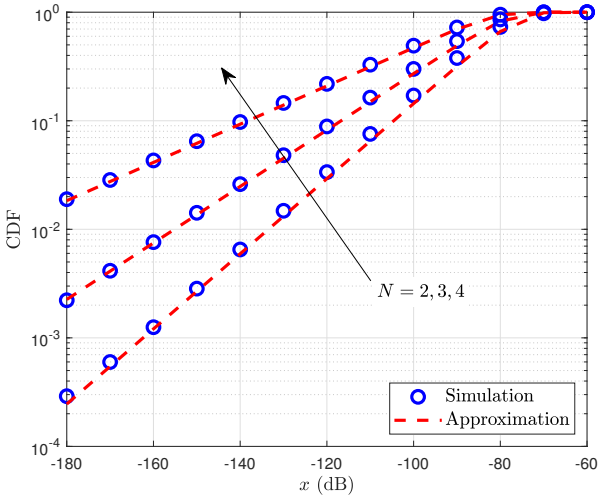

Fig. 3: Comparison between the exact THz channel CDF and the approximate gamma CDF with optimal ϵ_n of multiple received PSDs.

B. SINR and SIR for a General Case

By adopting the gamma approximation with the optimal $\{\epsilon_n\}_{n=1}^N$ in the last subsection, the derived CDFs and PDFs of SINR and SIR for a general case can be verified. We take the $\mathcal{S}_3$ for the interference channels. The approximated CDF and PDF of SINR/SIR using the exact distributions of the target received PSD, that is, (26), (28), (36), and (37), are denoted as "Approximation", while the approximated CDF and PDF of SINR/SIR using the gamma approximated distribution of the target received PSD, that is, (32), (34), (38), and (40), are denoted by "Alternative Approximation". Observing from Fig. 4-Fig. 7, we can see that the "Approximation" and simulation results can match each other very well for various cases with different parameter setups, no matter in PDF plots or CDF plots, and SINR case or SIR case. However, there are small gaps between the "Alternative Approximation" numerical results and the "Approximation" results or simulation. Since only the adopted distribution for the target received PSD is different in two cases, the gap is caused by the small mismatch between the gamma distribution approximation and the exact THz channel distribution. It also shows that the mismatch is negligible for the cases with multiple received signals. Although the "Alternative Approximation" does not match with the exact results as well as the "Approximation", it involves much simpler expressions and is more suited for practical calculation with stringent timing requirements. Meanwhile, these simulation results also verify the correctness of our derivation and the effectiveness of the gamma distribution approximation.

Moreover, the small-scale fading parameter m_{g_n} plays a positive role in channel condition as shown in Fig. 4. However, the increase of m_{g_0} does not bring much improvement in SINR for the co-channel interference channel model especially when m_{g_0} is large. As shown in Fig. 5, the CDF plots with $m_{g_0} = 3$ and $m_{g_0} = 6$ are almost overlap. The difference between the

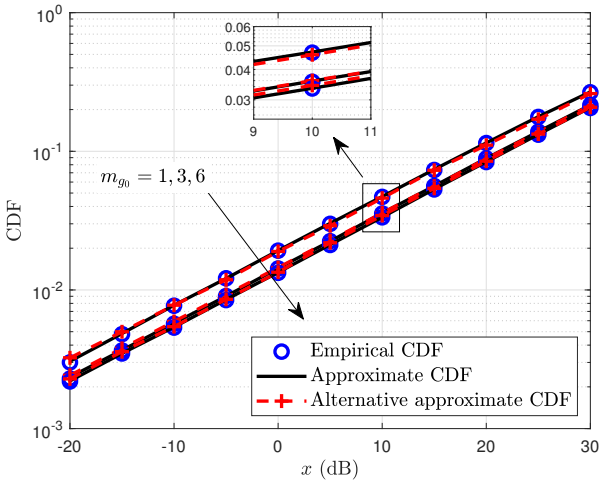

Fig. 4: CDF plots of SINR with different values of m_{g_0}.

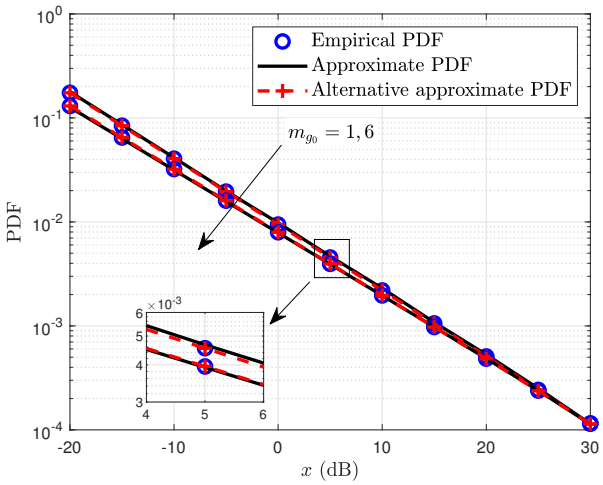

Fig. 5: PDF plots of SINR with different values of m_{g_0}.

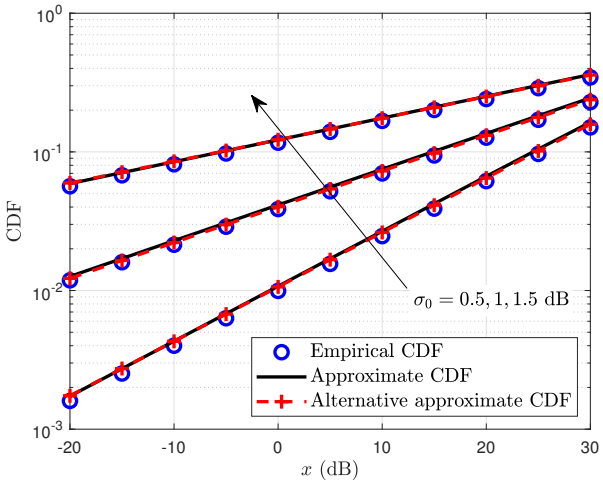

Fig. 6: CDF plots of SIR with different values of σ_0.

CDF plots with $m_{g_0} = 3$ and $m_{g_0} = 6$ is much smaller than

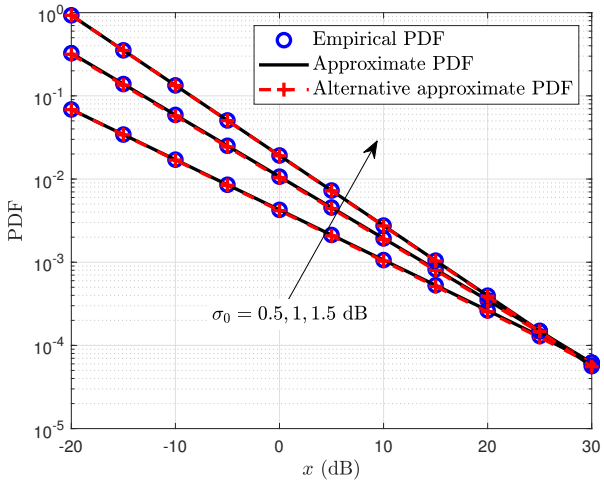

Fig. 7: PDF plots of SIR with different values of σ_0.

the one between the CDF plots with $m_{g_0} = 1$ and $m_{g_0} = 3$. It implies that the way to improve the scattering environment is not preferred to improve the co-channel interference system performance when the scattering environment has already been good enough. On the other hand, as presented in Fig. 6 and 7, the shadowing figure σ_n plays a negative role in the received PSD. The variation in the shadowing parameter would make a big difference in the quality of the received signal. That is to say, the shadowing condition plays a more important role for the radio transmissions over the THz band than the fading condition.

C. SINR and SIR for Special Cases

Finally, we verify our analytical results for the special cases by examining the CDF and PDF of SINR. The distance for cases with a single interferer and multiple i.i.d. interferers is configured to be $\{d_n\}_{n=1}^{N} = 3$ m. The derived exact CDF and PDF using the exact distributions of interferers and target users are denoted by "Analysis" in the figures. The two kinds of approximated results obtained from the general case can also be simplified for these special cases by re-configuring the parameters of the gamma distribution, which are also shown in Figs. 8-11. It can be summarized from the results presented in these figures that all the derived results match the simulation very well, which proves the correctness of our derivation once again. As can also be shown in Fig. 8 and 9, the system performance cannot be improved greatly with reduced medium absorption coefficient K_{A_0}, which indicates that the propagation environment does not play a significant role in THz communications. As observed from Fig. 10 and 11, the THz band is suitable for wireless communications over a short transmission distance. Moreover, the impact of the distance on the THz communication considering co-channel interference gradually decreases, which is same as the results shown in Fig. 2. For the case with multiple i.i.d. interferers and the identical shadowing factor, the approximated and alternative approximated results are not suitable anymore. However, its analytical form is similar to the one for the single-interferer

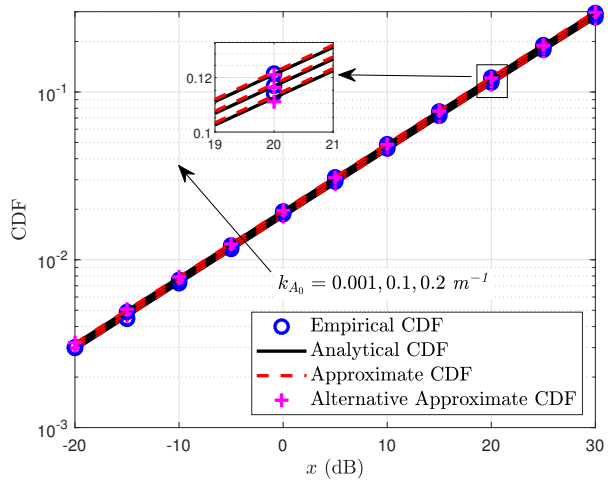

Fig. 8: CDF plots of SINR for the single-interferer cases with different values of k_{A_0}.

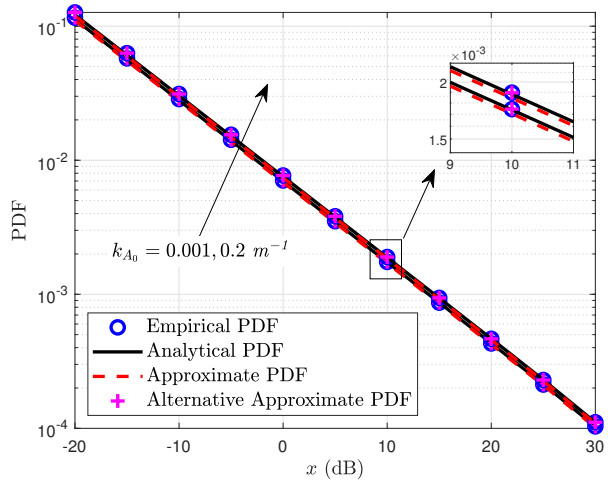

Fig. 9: The PDF plots for SINR for single-interferer cases with different values of k_{A_0}.

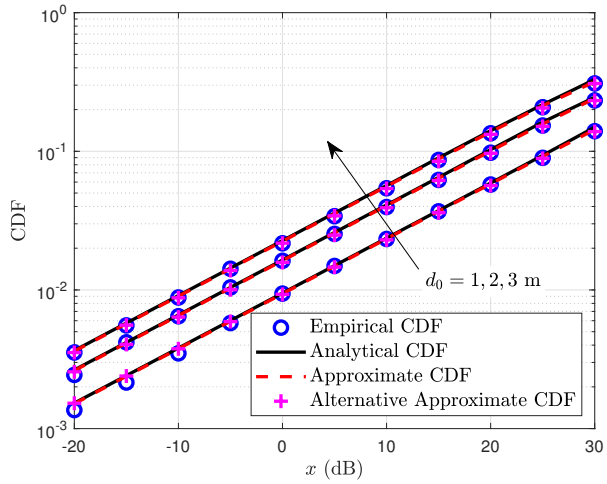

Fig. 10: CDF plots of SIR for the cases with multiple i.i.d. interferers with non-identical shadowing factors.

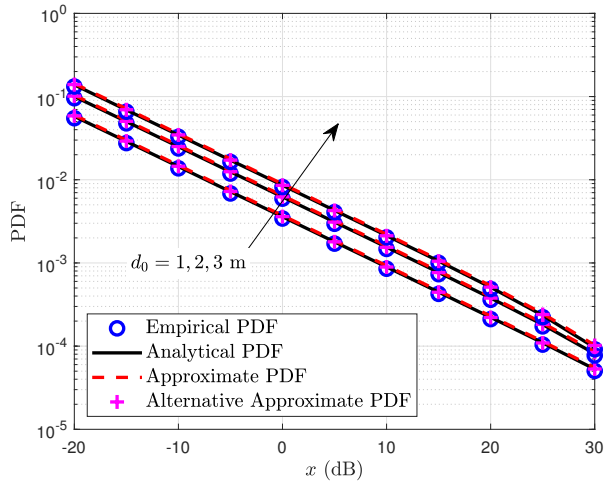

Fig. 11: PDF plots of SIR for the cases with multiple i.i.d. interferers with non-identical shadowing factors.

case. As a direct consequence of this similarity, the single-interferer case can be treated as a special case when $N = 1$. In addition, the analytical results and the simulation results shown in Fig. 12 and 13 match each others very well.

Moreover, we can also find from the presented results that the existence of the interferers seriously degrades the communication quality in the THz band. The interference cancellation should be an important and necessary research direction for realizing THz wireless communication systems in practice.

VI. Conclusion and Future Research Directions

In this paper, we investigated the SINR and SIR distributions for THz communication systems, considering the existence of co-channel interference, which is caused by frequency reuse. The analysis is general and has the potential to accelerate the PHY research progress on THz communications. The adopted channel model captures the realistic and important impacts of the THz propagation environment, including the molecular absorption loss, spreading loss, dynamic shadowing, and multi-path fading. Although the PDFs and CDFs of SINR and SIR are derived by approximating the distribution of the sum of interference as a gamma distribution with the MLE method, they have been proven to be a good fit through the numerical results. Furthermore, the exact and approximate analytical PDFs and CDFs expressions for the special cases considering a single interferer and multiple i.i.d. interferers were also derived. The simplicity and mathematical tractability of the co-channel interference model are expected to considerably facilitate advanced analyses and interference cancellation designs for THz communication systems. In particular, employing the system model with interference and the proposed analysis can measure the SINR/SIR and capture the performance of most THz communication systems subject to co-channel interference.

Although the considered scenario in this work may be

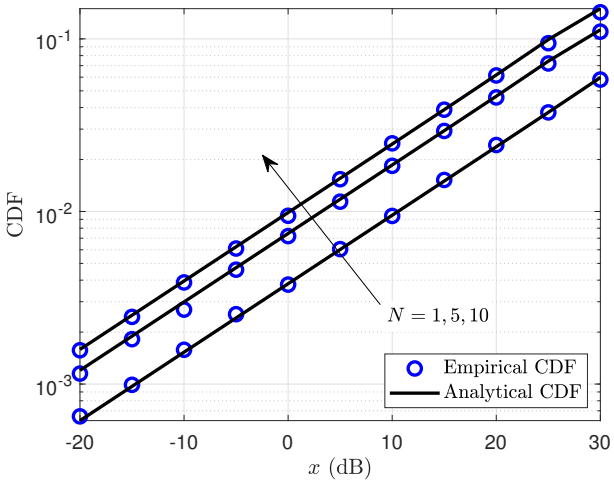

Fig. 12: CDF plots of SIR for the cases with multiple i.i.d. interferers with an identical shadowing factor.

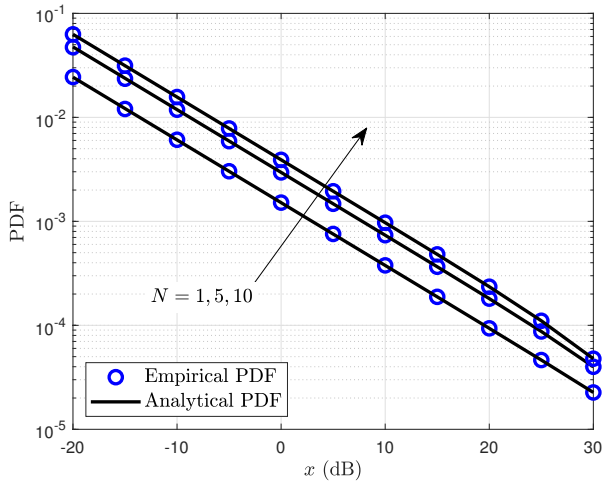

Fig. 13: CDF plots of SIR for the cases with multiple i.i.d. interferers with an identical shadowing factor.

thought of as an ideal case, the closed-form analytical expression derivations for the co-channel interference system performance rely on the assumptions of small transmission bandwidth and flat fading. Actually, it is an ideal assumption because the channels in the THz band are highly frequency-selective, and there are a large number of transmission windows caused by the molecular absorption. Moreover, the effects of misalignment, hardware impairments, and user equipment mobility on the THz communication system with co-channel interference have also not been investigated. The analysis and derivation under these more practical assumptions will be left for our future work, which tends to incorporate more conditions and constraints in practical implementation.

Moreover, this work only considers the classical communication scenario in the absence of other advanced auxiliary communication and networking technologies. For example, the performance and the achievable coverage area of THz systems can be enhanced by RISs, equipped with multiple passive reflecting patterns to introduce controllable scattering synthesis and enable multi-casting. The RIS technology can be utilized in both frequency-flat and frequency-selective fading channels by judiciously designing its reflection coefficients to increase the desired signal strength or mitigate the co-channel interference. Therefore, it is also a meaningful research direction to study the SINR and SIR of the co-channel interference THz system assisted by RISs with the adopted channel model in this work. The performance and properties of co-channel interfered THz system integrated with ultra-massive multiple input multiple output antenna array processing techniques supporting efficient beamforming for NLoS propagation, non-orthogonal multiple access techniques, and other promising technologies are still awaiting exploration. Furthermore, since the influence of moisture is imperceptible at high altitudes, the absorption loss of the THz-band is negligible, and THz communications can provide a much higher bandwidth and data rate for the communications among unmanned aerial vehicles, high altitude platforms, and up to the orbiting satellites. These promising advantages also motivate us to study the performance of densely deployed aerial communication networks with co-channel interference in future work.

ACKNOWLEDGMENT

The authors thank Prof. Josep M. Jornet with Northeastern University, USA, and Prof. Chong Han with Shanghai Jiao Tong University, China, for providing programs and data of the classic THz channel model, which are used in this paper for generating interference channel realizations.

REFERENCES

[1] S. Dang, O. Amin, B. Shihada, and M.-S. Alouini, "What should 6G be?" *Nature Electronics*, vol. 3, no. 1, pp. 20–29, 2020.

[2] Z. Ding, Y. Liu, J. Choi, Q. Sun, M. Elkashlan, C. I, and H. V. Poor, "Application of non-orthogonal multiple access in LTE and 5G networks," *IEEE Communications Magazine*, vol. 55, no. 2, pp. 185–191, 2017.

[3] E. Basar, M. Wen, R. Mesleh, M. Di Renzo, Y. Xiao, and H. Haas, "Index modulation techniques for next-generation wireless networks," *IEEE Access*, vol. 5, pp. 16 693–16 746, 2017.

[4] J. Li, Y. Peng, Y. Yan, X. Jiang, H. Hai, and M. Zukerman, "Cognitive radio network assisted by OFDM with index modulation," *IEEE Transactions on Vehicular Technology*, vol. 69, no. 1, pp. 1106–1110, 2020.

[5] M. Dohler, R. W. Heath, A. Lozano, C. B. Papadias, and R. A. Valenzuela, "Is the PHY layer dead?" *IEEE Communications Magazine*, vol. 49, no. 4, pp. 159–165, 2011.

[6] H. Song and T. Nagatsuma, "Present and future of terahertz communications," *IEEE Transactions on Terahertz Science and Technology*, vol. 1, no. 1, pp. 256–263, 2011.

[7] C. M. Armstrong, "The truth about terahertz," *IEEE Spectrum*, vol. 49, no. 9, pp. 36–41, 2012.

[8] I. F. Akyildiz, J. M. Jornet, and C. Han, "Terahertz band: Next frontier for wireless communications," *Physical Communication*, vol. 12, pp. 16–32, 2014.

[9] I. F. Akyildiz, J. M. Jornet, and C. Han, "TeraNets: ultra-broadband communication networks in the terahertz band," *IEEE Wireless Communications*, vol. 21, no. 4, pp. 130–135, 2014.

[10] C. Han and Y. Chen, "Propagation modeling for wireless communications in the terahertz band," *IEEE Communications Magazine*, vol. 56, no. 6, pp. 96–101, 2018.

[11] K. M. S. Huq, S. A. Busari, J. Rodriguez, V. Frascolla, W. Bazzi, and D. C. Sicker, "Terahertz-enabled wireless system for beyond-5G ultra-fast networks: A brief survey," *IEEE Network*, vol. 33, no. 4, pp. 89–95, 2019.

[12] Z. Chen, X. Ma, B. Zhang, Y. Zhang, Z. Niu, N. Kuang, W. Chen, L. Li, and S. Li, "A survey on terahertz communications," *China Communications*, vol. 16, no. 2, pp. 1–35, 2019.

[13] H. Elayan, O. Amin, B. Shihada, R. M. Shubair, and M.-S. Alouini, "Terahertz band: The last piece of RF spectrum puzzle for communication systems," *IEEE Open Journal of the Communications Society*, vol. 1, pp. 1–32, 2020.

[14] S. Priebe and T. Kurner, "Stochastic modeling of THz indoor radio channels," *IEEE Transactions on Wireless Communications*, vol. 12, no. 9, pp. 4445–4455, 2013.

[15] D. He, K. Guan, A. Fricke, B. Ai, R. He, Z. Zhong, A. Kasamatsu, I. Hosako, and T. Kürner, "Stochastic channel modeling for kiosk applications in the terahertz band," *IEEE Transactions on Terahertz Science and Technology*, vol. 7, no. 5, pp. 502–513, 2017.

[16] K. Guan, G. Li, T. Kürner, A. F. Molisch, B. Peng, R. He, B. Hui, J. Kim, and Z. Zhong, "On millimeter wave and THz mobile radio channel for smart rail mobility," *IEEE Transactions on Vehicular Technology*, vol. 66, no. 7, pp. 5658–5674, 2017.

[17] K. Guan, B. Peng, D. He, J. M. Eckhardt, S. Rey, B. Ai, Z. Zhong, and T. Kurner, "Channel characterization for intra-wagon communication at 60 and 300 GHz bands," *IEEE Transactions on Vehicular Technology*, vol. 68, no. 6, pp. 5193–5207, 2019.

[18] K. Guan, B. Peng, D. He, J. M. Eckhardt, S. Rey, B. Ai, Z. Zhong, and T. Kürner, "Measurement, simulation, and characterization of train-to-infrastructure inside-station channel at the terahertz band," *IEEE Transactions on Terahertz Science and Technology*, vol. 9, no. 3, pp. 291–306, 2019.

[19] D. He, B. Ai, K. Guan, L. Wang, Z. Zhong, and T. Kürner, "The design and applications of high-performance ray-tracing simulation platform for 5G and beyond wireless communications: A tutorial," *IEEE Communications Surveys Tutorials*, vol. 21, no. 1, pp. 10–27, 2019.

[20] L. Xu, M. Chen, M. Chen, Z. Yang, C. Chaccour, W. Saad, and C. S. Hong, "Joint location and power optimization for thz-enabled uav communications," *arXiv preprint arXiv:2011.01065*, 2020.

[21] A. Saeed, O. Gurbuz, and M. A. Akkas, "Terahertz communications at various atmospheric altitudes," *Physical Communication*, vol. 41, p. 101113, 2020.

[22] C. Huang, Z. Yang, G. C. Alexandropoulos, K. Xiong, L. Wei, C. Yuen, and Z. Zhang, "Hybrid beamforming for ris-empowered multi-hop terahertz communications: A drl-based method," *arXiv preprint arXiv:2009.09380*, 2020.

[23] H. Sarieddeen, M.-S. Alouini, and T. Y. Al-Naffouri, "An overview of signal processing techniques for terahertz communications," *arXiv preprint arXiv:2005.13176*, 2020.

[24] Z. Liu, J. Liu, Y. Zeng, and J. Ma, "Covert wireless communication in iot network: From awgn channel to thz band," *IEEE Internet of Things Journal*, vol. 7, no. 4, pp. 3378–3388, 2020.

[25] J. M. Williams, R. Khanna, J. P. Ruiz-Rosero, G. Pisharody, Y. Qian, C. R. Carlson, H. Liu, and G. Ramirez-Gonzalez, "Weaving the wireless web: Toward a low-power, dense wireless sensor network for the industrial IoT," *IEEE Microwave Magazine*, vol. 18, no. 7, pp. 40–63, 2017.

[26] S. Dang, J. Li, M. Wen, S. Mumtaz, and Z. Zhang, "OFDM-IM based dual-hop system using fixed-gain amplify-and-forward relay with pre-processing capability," *IEEE Transactions on Wireless Communications*, vol. 18, no. 4, pp. 2259–2270, 2019.

[27] J. Kokkoniemi, J. Lehtomäki, and M. Juntti, "Stochastic geometry analysis for mean interference power and outage probability in THz networks," *IEEE Transactions on Wireless Communications*, vol. 16, no. 5, pp. 3017–3028, 2017.

[28] A. A. Boulogeorgos, A. Alexiou, T. Merkle, C. Schubert, R. Elschner, A. Katsiotis, P. Stavrianos, D. Kritharidis, P. Chartsias, J. Kokkoniemi, M. Juntti, J. Lehtomaki, A. Teixeira, and F. Rodrigues, "Terahertz technologies to deliver optical network quality of experience in wireless systems beyond 5G," *IEEE Communications Magazine*, vol. 56, no. 6, pp. 144–151, 2018.

[29] V. Petrov, J. Kokkoniemi, D. Moltchanov, J. Lehtomaki, Y. Koucheryavy, and M. Juntti, "Last meter indoor terahertz wireless access: Performance insights and implementation roadmap," *IEEE Communications Magazine*, vol. 56, no. 6, pp. 158–165, 2018.

[30] I. F. Akyildiz and J. M. Jornet, "The Internet of nano-things," *IEEE Wireless Communications*, vol. 17, no. 6, pp. 58–63, 2010.

[31] C. Han and I. F. Akyildiz, "Distance-aware bandwidth-adaptive resource allocation for wireless systems in the terahertz band," *IEEE Transactions on Terahertz Science and Technology*, vol. 6, no. 4, pp. 541–553, 2016.

[32] J. M. Jornet and I. F. Akyildiz, "Low-weight channel coding for interference mitigation in electromagnetic nanonetworks in the terahertz band," in *Proc. IEEE International Conference on Communications (ICC)*, Kyoto, Japan, 2011, pp. 1–6.

[33] ——, "Information capacity of pulse-based wireless nanosensor networks," in *Proc. Annual IEEE Communications Society Conference on Sensor, Mesh and Ad Hoc Communications and Networks*, Salt Lake City, UT, USA, 2011, pp. 80–88.

[34] ——, "Joint energy harvesting and communication analysis for perpetual wireless nanosensor networks in the terahertz band," *IEEE Transactions on Nanotechnology*, vol. 11, no. 3, pp. 570–580, 2012.

[35] R. Indrawijaya and T. Kürner, "Simulation of terahertz intrabody wireless nano sensor networks in the presence of noise and interference," in *Proc. IEEE European Conference on Antennas and Propagation (EuCAP)*, London, UK, 2018, pp. 1–5.

[36] V. Petrov, D. Moltchanov, and Y. Koucheryavy, "Interference and SINR in dense terahertz networks," in *Proc. IEEE Vehicular Technology Conference (VTC2015-Fall)*, Boston, MA, USA, 2015, pp. 1–5.

[37] ——, "On the efficiency of spatial channel reuse in ultra-dense THz networks," in *Proc. IEEE Global Communications Conference (GLOBECOM)*, San Diego, CA, USA, 2015, pp. 1–7.

[38] V. Petrov, M. Komarov, D. Moltchanov, J. M. Jornet, and Y. Koucheryavy, "Interference and SINR in millimeter wave and terahertz communication systems with blocking and directional antennas," *IEEE Transactions on Wireless Communications*, vol. 16, no. 3, pp. 1791–1808, 2017.

[39] C. Wang, X. Yao, C. Han, and W. Wang, "Interference and coverage analysis for terahertz band communication in nanonetworks," in *Proc. IEEE Global Communications Conference (GLOBECOM)*, Singapore, 2017, pp. 1–6.

[40] V. Petrov, J. Kokkoniemi, D. Moltchanov, J. Lehtomäki, M. Juntti, and Y. Koucheryavy, "The impact of interference from the side lanes on mmWave/THz band V2V communication systems with directional antennas," *IEEE Transactions on Vehicular Technology*, vol. 67, no. 6, pp. 5028–5041, 2018.

[41] C. Chaccour, R. Amer, B. Zhou, and W. Saad, "On the reliability of wireless virtual reality at terahertz (THz) frequencies," in *Proc. IFIP International Conference on New Technologies, Mobility and Security (NTMS)*, Canary Islands, Spain, 2019, pp. 1–5.

[42] Z. Hossain, C. N. Mollica, J. F. Federici, and J. M. Jornet, "Stochastic interference modeling and experimental validation for pulse-based terahertz communication," *IEEE Transactions on Wireless Communications*, vol. 18, no. 8, pp. 4103–4115, 2019.

[43] Y. Wu and C. Han, "Interference and coverage analysis for indoor terahertz wireless local area networks," in *Proc. IEEE Globecom Workshops*, Waikoloa, HI, USA, 2019, pp. 1–6.

[44] S. Al-Ahmadi, "The gamma-gamma signal fading model: A survey [wireless corner]," *IEEE Antennas and Propagation Magazine*, vol. 56, no. 5, pp. 245–260, 2014.

[45] P. M. Shankar, "Outage probabilities in shadowed fading channels using a compound statistical model," *IEE Proceedings - Communications*, vol. 152, no. 6, pp. 828–832, 2005.

[46] I. M. Kostic, "Analytical approach to performance analysis for channel subject to shadowing and fading," *IEE Proceedings - Communications*, vol. 152, no. 6, pp. 821–827, 2005.

[47] I. Trigui, A. Laourine, S. Affes, and A. Stephenne, "Outage analysis of wireless systems over composite fading/shadowing channels with co-channel interference," in *Proc. IEEE Wireless Communications and Networking Conference (WCNC)*, Budapest, Hungary, 2009, pp. 1–6.

[48] ——, "Performance analysis of mobile radio systems over composite fading/shadowing channels with co-located interference," *IEEE Transactions on Wireless Communications*, vol. 8, no. 7, pp. 3448–3453, 2009.

[49] S. Al-Ahmadi and H. Yanikomeroglu, "On the approximation of the PDF of the sum of independent generalized-K RVs by another generalized-K PDF with applications to distributed antenna systems," in *Proc. IEEE Wireless Communication and Networking Conference*, Sydney, NSW, Australia, 2010, pp. 1–6.

[50] S. Kusaladharma and C. Tellambura, "Aggregate interference analysis for underlay cognitive radio networks," *IEEE Wireless Communications Letters*, vol. 1, no. 6, pp. 641–644, 2012.

[51] P. S. Bithas and A. A. Rontogiannis, "Mobile communication systems in the presence of fading/shadowing, noise and interference," *IEEE Transactions on Communications*, vol. 63, no. 3, pp. 724–737, 2015.

[52] N. Bhargav, C. R. N. da Silva, Y. J. Chun, S. L. Cotton, and M. D. Yacoub, "Co-channel interference and background noise in κ - μ fading channels," *IEEE Communications Letters*, vol. 21, no. 5, pp. 1215–1218, 2017.

[53] J. Kokkoniemi, J. Lehtomäki, and M. Juntti, "A discussion on molecular absorption noise in the terahertz band," *Nano communication networks*, vol. 8, pp. 35–45, 2016.

[54] S. Al-Ahmadi and H. Yanikomeroglu, "On the approximation of the generalized-k distribution by a gamma distribution for modeling composite fading channels," *IEEE Transactions on Wireless Communications*, vol. 9, no. 2, pp. 706–713, 2010.

[55] I. J. Myung, "Tutorial on maximum likelihood estimation," *Journal of mathematical Psychology*, vol. 47, no. 1, pp. 90–100, 2003.

[56] J. Nocedal and S. Wright, *Numerical optimization*. Springer Science & Business Media, 2006.

[57] I. S. Gradshteyn and I. M. Ryzhik, *Table of Integrals, Series, and Products*. Academic Press, 2014.

[58] S. Dang, G. Chen, and J. P. Coon, "Multicarrier relay selection for full-duplex relay-assisted OFDM D2D systems," *IEEE Transactions on Vehicular Technology*, vol. 67, no. 8, pp. 7204–7218, 2018.

[59] O. El Ayach, S. W. Peters, and R. W. Heath, "The feasibility of interference alignment over measured MIMO-OFDM channels," *IEEE Transactions on Vehicular Technology*, vol. 59, no. 9, pp. 4309–4321, 2010.

[60] M.-S. Alouini and A. J. Goldsmith, "Area spectral efficiency of cellular mobile radio systems," *IEEE Transactions on Vehicular Technology*, vol. 48, no. 4, pp. 1047–1066, 1999.

[61] N. D. Chatzidiamantis and G. K. Karagiannidis, "On the distribution of the sum of gamma-gamma variates and applications in RF and optical wireless communications," *IEEE Transactions on Communications*, vol. 59, no. 5, pp. 1298–1308, 2011.

[62] I. Trigui, A. Laourine, S. Affes, and A. Stéphenne, "Outage analysis of wireless systems over composite fading/shadowing channels with co-channel interference," in *2009 IEEE Wireless Communications and Networking Conference*. IEEE, 2009, pp. 1–6.

[63] S. Kim and A. G. Zajić, "A path loss model for 300-ghz wireless channels," in *2014 IEEE Antennas and Propagation Society International Symposium (APSURSI)*. IEEE, 2014, pp. 1175–1176.

[64] Y. Wu and C. Han, "Interference and coverage analysis for indoor terahertz wireless local area networks," in *2019 IEEE Globecom Workshops (GC Wkshps)*. IEEE, 2019, pp. 1–6.

[65] J. Sayehvand and H. Tabassum, "Interference and coverage analysis in coexisting rf and dense terahertz wireless networks," *IEEE Wireless Communications Letters*, vol. 9, no. 10, pp. 1738–1742, 2020.